Bit-Interleaved Coded Modulation for Hybrid RF/FSO Systems

by

Xiaohui He

B.ENG., McMaster University, 2005

A THESIS SUBMITTED IN PARTIAL FULFILLMENT OF
THE REQUIREMENTS FOR THE DEGREE OF

MASTER OF APPLIED SCIENCE

in

THE FACULTY OF GRADUATE STUDIES

(Electrical and Computer Engineering)

THE UNIVERSITY OF BRITISH COLUMBIA

Vancouver

December 2008

Abstract

In this thesis, we propose a novel architecture for hybrid radio frequency (RF)/free–space optics (FSO) wireless systems. Hybrid RF/FSO systems are attractive since the RF and FSO sub–systems are affected differently by weather and fading phenomena. We give a thorough introduction to the RF and FSO technology, respectively. The state of the art of hybrid RF/FSO systems is reviewed. We show that a hybrid system robust to different weather conditions is obtained by joint bit–interleaved coded modulation (BICM) of the bit streams transmitted over the RF and FSO sub–channels. An asymptotic performance analysis reveals that a properly designed convolutional code can exploit the diversity offered by the independent sub–channels. Furthermore, we develop code design and power assignment criteria and provide an efficient code search procedure. The cut–off rate of the proposed hybrid system is also derived and compared to that of hybrid systems with perfect channel state information at the transmitter. Simulation results show that hybrid RF/FSO systems with BICM outperform previously proposed hybrid systems employing a simple repetition code and selection diversity.

Contents

List of Figures

List of Abbreviations and Symbols

Acronyms

AP	Assignment pattern
AWGN	Additive white Gaussian noise
BICM	Bit-interleaved coded modulation
CC	Convolutional code
CEP	Codeword error probability
CSI	Channel state information
EDFA	Erbium doped fiber amplifier
EIRP	Equivalent isotropic radiated power
FSO	Free-space optics
GTF	Generated transfer function
IM/DD	Intensity modulation and direct detection
LD	Laser diode
LDPC	Low density parity check
LED	Light-emitting diode
MIMO	multiple input multiple output
MMW	Millimeter wave
OOK	On-off keying
pdf	Probability density function
PEP	Pairwise error probability

QAM	Quadrature amplitude modulation
RC-SD	Repetition code and selection diversity
RF	Radio frequency
S.I.	Scintillation index
SNR	Signal-to-noise ratio
VD	Viterbi decoder

Operators and Notations

$\lvert\cdot\rvert$	Absolute value of a complex number
$\cdot \otimes \cdot$	Convolution
$\delta(\cdot)$	Dirac delta function
$\mathcal{E}\{\cdot\}$	Expectation
$\det(\cdot)$	Determinant
$\mathrm{tr}(\cdot)$	Trace
$[\cdot]^*$	Complex conjugate
$[\cdot]^T$	Matrix or vector transposition
$[\cdot]^H$	Matrix or vector Hermitian transposition
$[x]^+$	$\max(x, 0)$
$\mathbf{0}_m$	All–zero column vector of length m
$\boldsymbol{I}_m$	Identity matrix with dimension $m \times m$
$I_n(\cdot)$	The modified Bessel function of the first kind and n-th order

Acknowledgments

Firstly and foremost, I would like to take this chance to give my warm and grateful thanks to my supervisor, Dr. Robert Schober, for providing me with the opportunity to work in the field of free space optics and wireless communication, and nurturing my knowledge with amazing generosity and patience. I always benefited from his overall guidance, and support of my future career.

I would also like to extend my thanks to the people I have met at UBC Data Communication Lab during my research: Yangwen Liang, Harry Chen, Ali Nezampour, Ehsan Bayaki, and others, for their help and encouragement. Sometimes they have shared the knowledge with me, some other times they have just provided moral support to me but, one way or the other, they have always been most helpful.

Finally, I would like to thank my family. They gracefully endured these years of voluntary exile in Vancouver and gave me their unlimited support.

Xiaohui He

The University of British Columbia
Vancouver, Canada
September 2008

Chapter 1

Introduction

The following section provides an overview of the background information and motivation for this work. We also review the related work that has been proposed by other researchers in this field. The contributions of this work are briefly summarized in the second section of this chapter, and the concluding section outlines the organization of the thesis.

1.1 Background and Motivation

Free–space optics (FSO) and millimeter wave (MMW) radio frequency (RF) systems have received considerable attention for high rate (e.g. 100 Mbit/s–10 Gbit/s) wireless communication over distances of up to a few kilometers [2]–[5]. Besides the high data rates, FSO and 60–GHz RF systems offer similar advantages such as flexibility of deployment, license–free operation, and inherent security due to high link attenuation. However, both technologies are affected quite differently by atmospheric and weather effects. FSO links suffer from extremely high attenuation in the presence of fog but are less affected by rain. In contrast, fog has practically no effect on 60–GHz systems but rain significantly increases link attenuation. Similarly, while atmospheric turbulence caused by variations in the refractive index is the main cause of small–scale fading in FSO links [6, 7], RF links are impaired by Rayleigh or Ricean fading

due to multipath propagation [4, 8, 9].

The complementary nature of FSO and RF channels has led to various proposals for hybrid RF/FSO systems. The combination of high–rate FSO with low–rate RF systems operating in the 2.4 GHz frequency band was proposed in [10] and experimentally validated in [11, 12]. However, ultimately the achievable data rate of this type of hybrid system is limited by the small RF bandwidths available in the 2.4 GHz band. This problem can be overcome if the RF system operates in the MMW frequency band which supports data rates similar to those of FSO [13]–[15]. If channel state information (CSI) is available at the transmitter, a simple CSI–dependent switching between the FSO and the RF system can be applied [10]. An efficient coding scheme based on low density parity check codes for hybrid RF/FSO channels with CSI at the transmitter has been proposed in [16]. To avoid the overhead necessary for CSI acquisition and to be robust against instantaneous interruptions caused by e.g. bird fly–through in the FSO system, transmitting the same data over both links has been proposed in [13]. In this scheme, the receiver detects the data streams received over the FSO and the RF links independently, and selects that data stream which is deemed more reliable on a frame–by–frame basis. This approach may be viewed as a simple repetition code across both links. However, the complimentary nature of both links is still not fully exploited. More details about the scheme in [13] can be found in Section 2.3.

1.2 Contributions

In this thesis, we introduce a robust coding scheme for hybrid RF/FSO channels for the case when CSI is not available at the transmitter. From a communication theory point of view, the hybrid RF/FSO channel can be modeled as a *heterogeneous* block fading channel with two independent sub–channels having different fading statistics and favoring different modulation schemes. Coding for *homogeneous* block fading channels having identical statistical prop-

erties has been extensively studied in the literature [17, 18]. Bit–interleaved coded modulation (BICM) [19] was shown to achieve close–to–optimum performance in this type of channel [20] and efficient code designs have been reported [21, 22]. As will be shown in this thesis, BICM is also well suited for the heterogeneous block fading channel typical for hybrid RF/FSO systems. In particular, its convenient separation of coding and modulation facilitates the application of different modulation schemes over the RF and FSO sub–channels.

The main contributions of the present research work are as follows:

- For the case when CSI is not available, a joint BICM scheme is designed for hybrid FSO/RF channels. Coded sequences are transmitted simultaneously over both channels according to a bit assignment pattern and combined via standard Viterbi decoding at the receivers. For FSO channel a Gamma-Gamma fading model is adopted, while Ricean fading is assumed for RF channel fading.
- Analytical expressions for the asymptotic pairwise error probability (PEP) and the asymptotic codeword error probability (CEP) are presented. In particular, union bounds for asymptotic PEP and CEP are derived. Bounds on code rates for both channels are determined. This is an extension of the work in [19]. In [19], PEP and CEP are derived when all parallel channels are identical. In our work, we extend the theory to nonidentical, heterogeneous parallel channels.
- Algorithms and computational methods for searching the optimum combination of code and assignment pattern for different code constraint lengths and pattern lengths are presented. Results are also presented.
- A cut-off rate analysis for the proposed joint BICM for FSO/RF channels is presented. A simulation comparison between the proposed design and independent BICM with CSI, shows that the cut-off rate of joint BICM is only slightly lower than that of independent BICM with CSI while the system complexity is greatly reduced because of the removal of CSI

estimation.

- The simulation results for the FER show that for a given bit rate, the proposed joint BICM scheme outperforms the scheme proposed in [13], namely repetition coding with selection diversity, as well as the scheme when only FSO channel is in use. We compare the performance under weather conditions such as clear air, haze and rain.

The results of our work are summarized in the following papers:

- B. He and R. Schober. Bit–Interleaved Coded Modulation for Hybrid RF/FSO Systems. *Accepted subject to revisions for publication in the IEEE Transactions on Wireless Communications*, July 2008.

- B. He and R. Schober. Bit-Interleaved Coded Modulation for Hybrid RF/FSO Systems. *Submitted to IEEE International Conference on Communication (ICC) 2009,Dresden, Germany*, July 2008.

1.3 Thesis Organization

To explain the above findings in detail, the thesis is organized as follows. In Chapter 2, an introduction to both FSO and 60-GHz MMW channels is given. Fading models for both types of channels are provided. In Chapter 3, the system model including transmitter and receiver structure is given. We describe the algorithm for joint code and assignment pattern search in Chapter 5. Search results are also presented in this section. The analysis of the cut-off rate for joint BICM hybrid RF/FSO systems is given in Chapter 6. Simulation results are provided in Chapter 7. The results also include comparisons between our joint BICM system and previously proposed systems. Finally, conclusions and discussion of future work are provided in Chapter 8.

Chapter 2

Introduction to FSO and 60-GHz RF

2.1 FSO Fundamentals

Free space optics (FSO) can be defined as unguided or wireless communications in the optical band emission, both coherently and incoherently. Historically, conveying information optically through the atmospheric channel was one of the most primitive forms of communication known to mankind. Classical examples include Euclid's *Optica* and Hero's *Catopricia* which discussed how the ancient Greeks used the sun's reflection from metal disks to signal over vast distances. In the 1790s, Claude Chappie invented the *Optical Telegraph* which uses a series of semaphores-mounted towers to relay messages from one to another. In 1880, Alexander Graham Bell used a *photophone* to transmit telephone signals via an intensity-modulated optical beam 200 m through air to a distant receiver.

The resurrection of modern optical communication can be associated with the invention of lasers in the late 1950s. The properties of laser radiation, such as monochrome, coherence, and intenseness, enable the possibility of transmitting high data rate at around 2.5 Gbps [1, 10].

Early development of unguided laser communication was directed towards

satellite and remote military applications. One example is the Low Earth Orbit (LEO) or the Geosynchronous (GEO) satellite-based communication system, with an optical link operating at a typical range of 45,000 km. Recently, although fiber-optic cabling is still the preferred media for long haul, high-bandwidth transport, its drawbacks such as high installation cost and the unremovable nature have opened a room for the development of commercial FSO research and deployment. Currently FSO is regarded as one of the most potent *last mile* technologies, and already deployed as point-to-point Giga bit connection for high-rise building. Other applications of FSO also include metropolitan area network extensions, enterprise/local area network connectivity, fiber backup, back-haul for wireless cellular networks, redundant link and disaster recovery [2, 3].

2.1.1 Brief Description of Optical Communication Systems

Figure 2.1 illustrates a conventional point-to-point FSO communication system [1]. The transmitter comprises a photoemitter, e.g., a laser diode (LD) or a light-emitting diode (LED), as light source, an erbium doped fiber amplifier (EDFA) which often has a wavelength around 980 nm and sometimes around 1550 nm,, and a telescope assembly. Input data is modulated by Intensity Modulation (IM), and carried by the emitted light from the photoemitter. The intensity, and hence the instantaneous power is proportional to the modulating current at the photoemitter. The power of the emitted light may be low and is usually amplified by an EDFA. The telescope can be designed by using either lenses or a parabolic mirror, and is used to narrow the light beam and to project it toward the receiver.

At the receiver side, the transmitted light is picked up using a lens or a mirror and then focused on a direct detection (DD) photodetector, e.g., a semiconductor photodiode, a PIN (P-type, intrinsic, N-type) diode, or an avalanche

photodiode (APD). An electrical current is generated by photoabsorption at a rate which is proportional to the instantaneous optical power incident on the active detector surface. The intrinsically discrete nature of the current gives rise to shot noise observed in low light level detection; additional shot noise results from external sources of radiation, called *background radiation*, as well as from spontaneously generated charge particles, called *dark current* [6]. The signal is hence determined by the photocurrent.

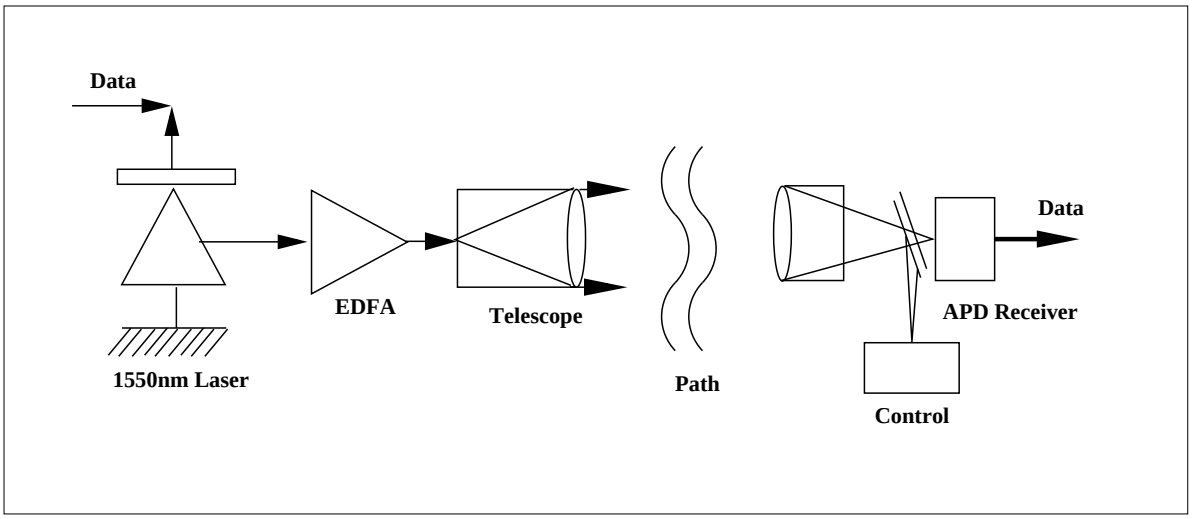

Figure 2.1: Schematic diagram of point-to-point FSO communication system[1].

2.1.2 Factors Affecting FSO

Several factors are associated with FSO link impairments and cause transmission power attenuation and degradation of system reliability. These factors include scintillation, obstruction, misalignment, weather effects, and window attenuation. For our research, we assume that a Line-of-Sight (LOS) link is always available. This is a practical assumption for most FSO applications. Also, we always assume perfect alignment. Hence in the following, we would focus on scintillation and weather effect.

Atmospheric Turbulence

In hot, dry climates, turbulence effects may degrade transmission performance. As the ground heats up in the sun, the air heats up as well. Some air cells or air pockets heat up more than others. This causes changes in the index of refraction, which in turn changes the path of light propagation. This fluctuation of the index of refraction results in atmospheric turbulence, also known as scintillation, and is a major reason of signal fading. In the literature, the normalized variance of intensity, more commonly known as *scintillation index* (S.I.), is used to denote the statistical characteristic of the light intensity [1]:

$$\text{S.I.} = \frac{\mathcal{E}\left\{I^2\right\}}{\left(\mathcal{E}\left\{I\right\}\right)^2} - 1 \tag{2.1}$$

Here I denotes the light intensity. In general, a low S.I. corresponds to less scattering, which .

Many statistical models for the intensity fluctuation in FSO channels have been proposed over the last two decades [7]. For weak turbulence, the log-normal distribution has been proposed as a suitable model for the intensity fluctuation. However, this model is not valid for strong turbulence. In recent research on FSO channel modeling, the Gamma-Gamma distribution was found more suitable for weak, medium and strong turbulence under various conditions [23, 7, 24]. More details will be given in Sub-section 2.1.3. Notice that the parameters which determine the fading models can be directly expressed in terms of the S.I.. It can be confidently expected that the error performance will degrade with increased S.I., as decision error events are typically correlated with low instantaneous fading intensity values.

Weather Effects

The FSO link quality is highly dependent on the weather conditions. FSO links suffer additional path loss under conditions such as rain, fog, and haze. The path loss due to low-visibility weather conditions is considered the major drawback in terms of reliability of FSO links and a significant barrier for

deployment. The path loss is a result of scattering and hence depends on the particle size and visibility in the atmosphere. For example, the impact of rain is significantly less than that of fog because the radius of rain drops (200-2000 μm) is significantly larger than the wavelength of typical FSO light source.

The attenuation of the laser power can be described by Beers-Lambert Law [25]

$$g_1\,[\mathrm{dB}] \triangleq a_1 L_1, \tag{2.2}$$

where a_1 denotes the weather–dependent attenuation coefficient (in dB/km) which varies depending on the weather, while L is the link distance.

The attenuation coefficient a_1 can be further expressed as a function of visibility V [km], the size distribution of the scattering particles q, and wavelength λ [km][26]:

$$a_1 = \frac{3.91}{V}\left(\frac{\lambda}{550\mathrm{nm}}\right)^{-q}, \tag{2.3}$$

The values of q depends on V:

$$q = \begin{cases} 1.6 & \text{for high visibility } (V > 50 \text{ km}) \\ 1.3 & \text{for average visibility } (6 \text{ km} < V < 50 \text{ km}) \\ 0.16V + 0.34 & \text{for haze visibility } (1 \text{ km} < V < 6 \text{ km}) \\ V - 0.5 & \text{for mist visibility } (0.5 \text{ km} < V < 1 \text{ km}) \\ 0 & \text{for fog visibility } (V < 0.5 \text{ km}) \end{cases} \tag{2.4}$$

For our case, we choose $\lambda = 1550$ nm as the FSO wavelength. According to 2.4, with V provided by [26], we can calculate the values of a_1 for clear air, haze, light fog, moderate fog, heavy fog, moderate rain and heavy rain are (in [dB/km]) 0.43, 4.2, 20, 42.2, 125, 5.8, and 9.2, respectively, see also Table 2.1 at the end of this chapter, which we summarize the parameters we used in for our later simulation.

2.1.3 FSO Fading Model

As mentioned in Section 2.1.2, we present two specific fading intensity models. Without loss of generality, all types of power density function (pdf) have been

normalized such that $\mu_I = \mathcal{E}\{I\} = 1$. Note that the distributions are only valid for $I \geq 0$.

Log-normal fading is the most widely accepted fading model for weak turbulence coditions. Its pdf is given by [27],[7]

$$p_I(I) = \frac{1}{I\sqrt{2\pi\sigma_x^2}} \exp\left(-\frac{(\ln(I) - m_x)^2}{2\sigma_x^2}\right) \tag{2.5}$$

Notice that, given a specific scintillation index, the distribution parameters are set according to $m_x = -0.5\ln(\text{S.I.} + 1)$ and $\sigma_x^2 = \ln(\text{S.I.} + 1)$, in order to satisfy $\mathcal{E}\{I\} = 1$.

The Gamma-Gamma fading distribution, a more recently proposed FSO fading intensity model, is considered to be more suitable for fading channels with moderate to strong turbulence, as well as weak turbulence. The fading is considered to be two stochastic processes, in which small-scale atmospheric fluctuations are modulated by large-scale fluctuations; both types of atmospheric fluctuations are modeled as being gamma distributed [23],[7]. The pdf of the intensity is given by

$$p_I(I) = \frac{2(\alpha\beta)^{(\alpha+\beta)/2}}{\Gamma(\alpha)\Gamma(\beta)} I^{(\alpha+\beta)/2-1} K_{\alpha-\beta}\left(2\sqrt{\alpha\beta I}\right), \qquad I \geq 0, \tag{2.6}$$

where $\Gamma\{\cdot\}$ is the gamma function, $K_v(\cdot)$ is the vth-order modified Bessel function of the second kind, and parameters $\alpha > 0$ and $\beta > 0$ can be adjusted to achieve a good agreement between $p_I(I)$ and measurement data for a wide range of turbulence conditions (weak to strong). Alternatively, assuming spherical wave propagation, α and β can be directly linked to physical parameters via [7, 23]

$$\alpha = \left[\exp\left(\frac{0.49\chi^2}{(1 + 0.18d^2 + 0.56\chi^{12/5})^{7/6}}\right) - 1\right]^{-1}, \tag{2.7}$$

$$\beta = \left[\exp\left(\frac{0.51\chi^2(1 + 0.69\chi^{12/5})^{-5/6}}{(1 + 0.9d^2 + 0.62d^2\chi^{12/5})^{5/6}}\right) - 1\right]^{-1}, \tag{2.8}$$

where

$$\chi^2 \triangleq 0.5C_n^2\kappa^{7/6}L^{11/6}, \tag{2.9}$$

$$d \triangleq (\kappa D^2/4L)^{1/2}, \tag{2.10}$$

and

$$\kappa \triangleq 2\pi/\lambda_1. \tag{2.11}$$

Here, λ_1 and D are the wavelength and the diameter of the receiver's aperture, respectively. C_n^2 stands for the altitude–dependent index of refraction structure parameter. Here we adapt the Hufnagel-Valley model [6] for C_n^2 profile model

$$\begin{aligned} C_n^2(h) &= 0.00594(v/27)^2(10^{-5}h)^{10}\exp(h/1000) \\ &\quad +2.7\times 10^{-6}\exp(-h/1500) + A\cdot\exp(-h/1000) \end{aligned} \tag{2.12}$$

where h is the altitude in meters (m), v is the rms windspeed in meters per second (m/sec) and A is a nominal value of $C_n^2(0)$ at the ground in $\mathrm{m}^{-2/3}$. For FSO links near the ground, C_n^2 can be taken approximately 1.7×10^{-14} $\mathrm{m}^{-2/3}$ during daytime and 8.4×10^{-15} $\mathrm{m}^{-2/3}$ at night. Generally, C_n^2 varies from 10^{-13} $\mathrm{m}^{-2/3}$ for strong turbulence to 10^{-17} $\mathrm{m}^{-2/3}$ for weak turbulence with 10^{-15} $\mathrm{m}^{-2/3}$ as a typical average value [28]. The scintillation index can be calculated from α and β according to

$$\text{S.I.} = \alpha^{-1} + \beta^{-1} + (\alpha\cdot\beta)^{-1} \tag{2.13}$$

For our research we adopt the Gamma-Gamma fading model for the rest of this thesis.

Figure 2.2 depicts sample pdf's of the log-normal fading model when S.I= 0.4 and the Gamma-Gamma fading model when S.I.= 0.88 .

2.2 60-GHz Millimeter-Wave Fundamentals

In response to the increasing demand for wireless bandwidth far in excess of the currently available bands at 2.4-2.5 and 5.2-5.8 GHz, in 2001, the Federal Communications Commission (FCC) allocated 7 GHz of bandwidth in the 57-64 GHz band for unlicensed use. This new allocation triggered great interest in developing affordable 60-GHz radios.

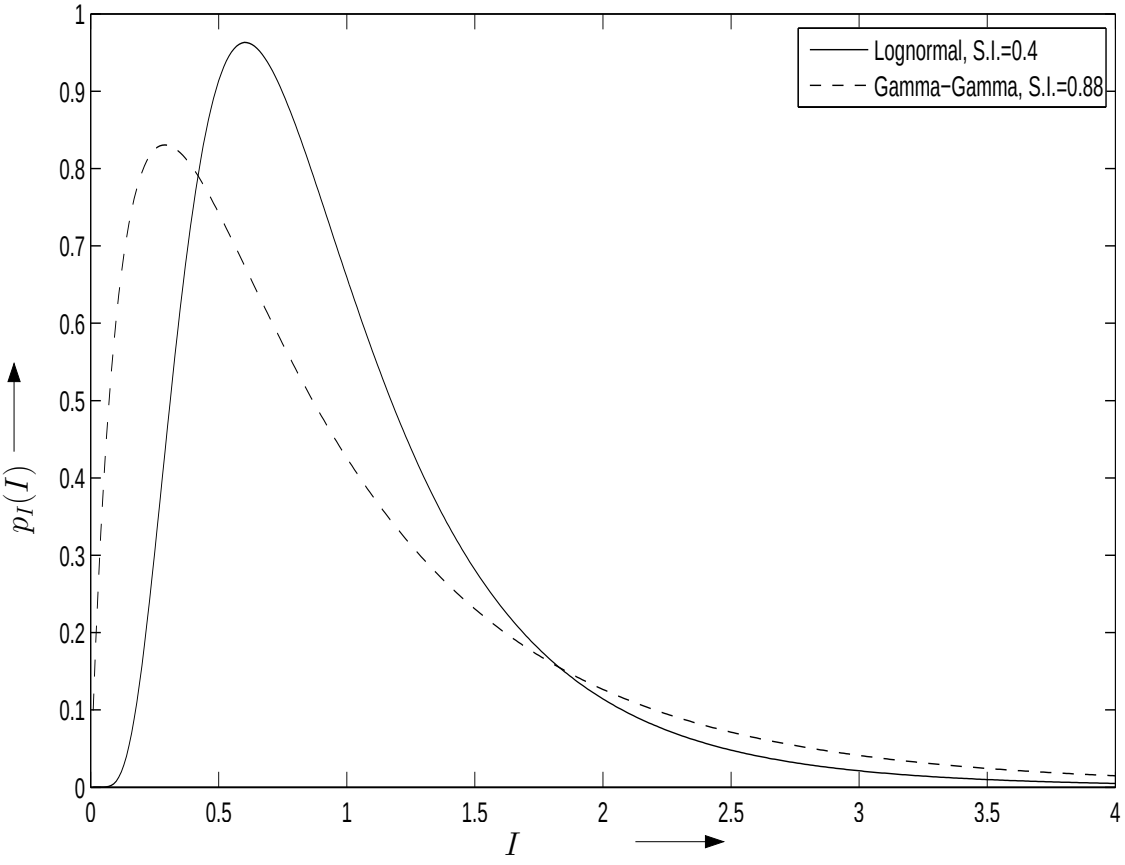

Figure 2.2: Sample log-normal and Gamma-Gamma fading intensity pdfs

2.2.1 Attraction of 60–GHz MMW

There are a few major benefits associated with the 60-GHz band.

Easy to deploy

First of all, the majority of the countries have allocated 7 GHz of continuous unlicensed spectrum at varying points between 57–66 GHz. For example, besides the USA, the spectrum allocations for Australia, Japan, and Europe are 59.4 GHz-62.9 GHz, 59 GHz-66 GHz, 57-66 GHz, respectively. More importantly, the 60-GHz band is unlicensed. Commercially, this means companies can deploy universal products globally and consumers can operate equipment in this band without purchasing a license.

Achievable high data rates

The 60-GHz band provides 5 GHz to 7 GHz available spectrum worldwide, and each of the channels shares 2500 MHz bandwidth, this is beyond the capacities of IEEE 801.11n (520 MHz) and UWB (40 MHz). Also, due to the oxygen absorption characteristics at 60 GHz, various regulators across Asia, Europe, and the Americas allow high Equivalent Isotropic Radiated Power (EIRP) for transmissions in this band. According to Shannon's Law [29]

$$C = B \cdot \log_2(1 + \text{SNR}) \quad \text{(b/s)} \tag{2.14}$$

where C, B and SNR denote the channel capacity, the bandwidth of the channel and the signal to noise ratio. The large bandwidth in the 60-GHz band, in addition to the high transmit power, enables data rates of up to 25,000 Mbps, which is much greater than 802.11n (1,100 Mbps) and UWB (80 Mbps) [30].

Interference-free and highly secure

Oxygen absorption has a peak around 60 GHz. This introduces benefits for 60 GHz and is one of the main reasons why this band is chosen due to its resis-

tance to interference. This is because that a particular radio link in this band is quickly reduced to a level that will not interfere with other 60-GHz links, giving the possibility of operating several 60-GHz devices at same location. In addition, radios operating at this frequency require high power to combat oxygen absorption, and hence the signals are typically very directional. Directivity is a measure of how well an antenna focuses its energy in an intended direction. A narrow beam sizes gives immunity to interference and interception.

2.2.2 60-GHz Band over 2.4-GHz and 5 GHz

In fact, 60-GHz is not the only license-free band. There are also other bands reserved internationally for the use of RF electromagnetic fields for industrial, scientific and medical (ISM) purposes other than communication [31]. The local wireless access based IEEE 802.11 standard operates in the 2.4-GHz and 5-GHz bands bandwidth of nearly 100 MHz and 150 MHz respectively [32]. In Europe, the high performance radio local area network (HIPERLAN) standard operates in the 5-GHz band [33]. The maximum net bit rates of these bands can be up to 54 Mbps for 802.11g [32] and HIPERLAN/2 [33]. However, there exists a multitude of multimedia applications calling for data rates up to a range of hundreds of megabits per second, which cannot be accommodated by current's local wireless access standards [34]. Examples include wireless TV (150-270 Mbps), wireless video conferencing (10-100 Mbps), and wireless IEEE 1394 (up to 400 Mbps) [34]. In principle, there are two ways to improve the channel capacity: increasing the spectral efficiency and/or using more bandwidth. spectral efficiency is defined as the amount of information that can be transmitted over a given bandwidth in a specific communication system, and is measure of how efficiently a limited frequency spectrum is utilized [34]. Methods to increase spectral efficiency include using higher order modulation methods are multiple transmitters/receivers with space-time coding. However, these improvements have tradeoff in different ways. For example, using higher order modulation comes with higher transmit power, while using multiple an-

tennas increases the complexity in terms of processing power and number of transceivers. If spectral efficiency stays about moderate level, increasing the bandwidth at a higher frequency is the only solution to higher data rates. This makes 60-GHz band the perfect solution for its up to 7 GHz bandwidth.

2.2.3 Atmospheric Absorption

In terms of large-scale fading and path loss, although there are losses due to phenomena such as water vapor, foliage, and vegetation [9], for 60-GHz channel, the major loss is due to oxygen absorption and rain attenuation.

Oxygen absorption

As mentioned before, oxygen absorption is a unique characteristic of the 60-GHz band. This gives the 60-GHz band some benefits, along with disadvantages such as path loss. The peak of oxygen absorption is very localized in frequency. The related attenuation can take high value near 60 GHz, and decreases by an order of magnitude when the frequency is near 66 GHz. For simplification, according to [35, 36], the path loss per distance can be modeled by an expression with respect to frequency f for the band 60 GHz–66 GHz with maximum error of 5%:

$$a_{\text{oxy}}[\text{dB/km}](f_{[\text{GHz}]}) = \begin{cases} 15.10 - 0.104 \times (f-60)^{3.26} & 60 \le f \le 63 \\ 11.35 + (f-60)^{2.25} - 5.33 \times (f-63)^{1.27} & 63 \le f \le 66 \end{cases} \tag{2.15}$$

In our calculation, we adopt 15.1 dB/km as the loss coefficient [9].

Rain attenuation

Clouds of ice crystals and snow do not cause appreciable attenuation [9]. However, when an electromagnetic wave propagates though a rain cell, it encounters a great amount of water droplets with different radii. The cumulative effect of electromagnetic wave penetration causes a considerable attenuation. Similar

to oxygen absorption, the per kilometer attenuation could also be modeled with respect to the rain fall rate R and frequency f [36]

$$\begin{aligned} & a_{\text{rain}}[\text{dB/km}](f_{[\text{GHz}]}) = a \times R^b \\ a = \;& 4.09 \cdot 10^{-2} f^{0.669} \quad \text{for} \quad 54 \leq f \leq 180 \\ b = \;& 2.63 f^{-0.272} \quad \text{for} \quad 25 \leq f \leq 164 \end{aligned} \tag{2.16}$$

In our model, we adopt 12.5 mm/h and 25 mm/h as the fall rate for moderate and heavy rain respectively [10]. The corresponding values of a_{rain} are 5.6 dB/km and 10.2 dB/km.

2.2.4 60-GHz MMW Fading Model

Small-scale fading in multipath channels occurs due to the incoherent superposition of a great number of multipath components, each having a different phase variation over time or frequency, or both. Among with all fading models used for 60 GHz in literature, the most popular models for possibly time-variant multipath channels are Rayleigh or Rice fading model [9]. The difference between Rayleigh distribution and Rice distribution is that Rayleigh models fading channels without line-of-sight (LOS) path, while Rice fading describes the case when there is a dominant incoming wave which is the LOS component. One can view the Rayleigh distribution as one extreme case of the Rice distribution when the dominant path is insignificant.

For simplicity, we assume the a LOS always exists since the FSO link requires a LOS. Hence, we choose the Rice distribution as our fading model and use it throughout this thesis.

If we denote $2\sigma_r^2$ the mean power of the sum of the non-specular (non-LOS) component and s^2 denotes the LOS component, then the pdf can be expressed as:

$$p_R(r) = \frac{r}{\sigma_r^2} \exp(-\frac{r^2 + s^2}{2\sigma_r^2}) \mathrm{I}_0(\frac{r \cdot s}{\sigma_r^2}), \quad r \in [0, \infty) \tag{2.17}$$

where $\mathrm{I}_{\mathrm{n}}(\cdot)$ denotes the modified Bessel function of the first kind and n-th order.

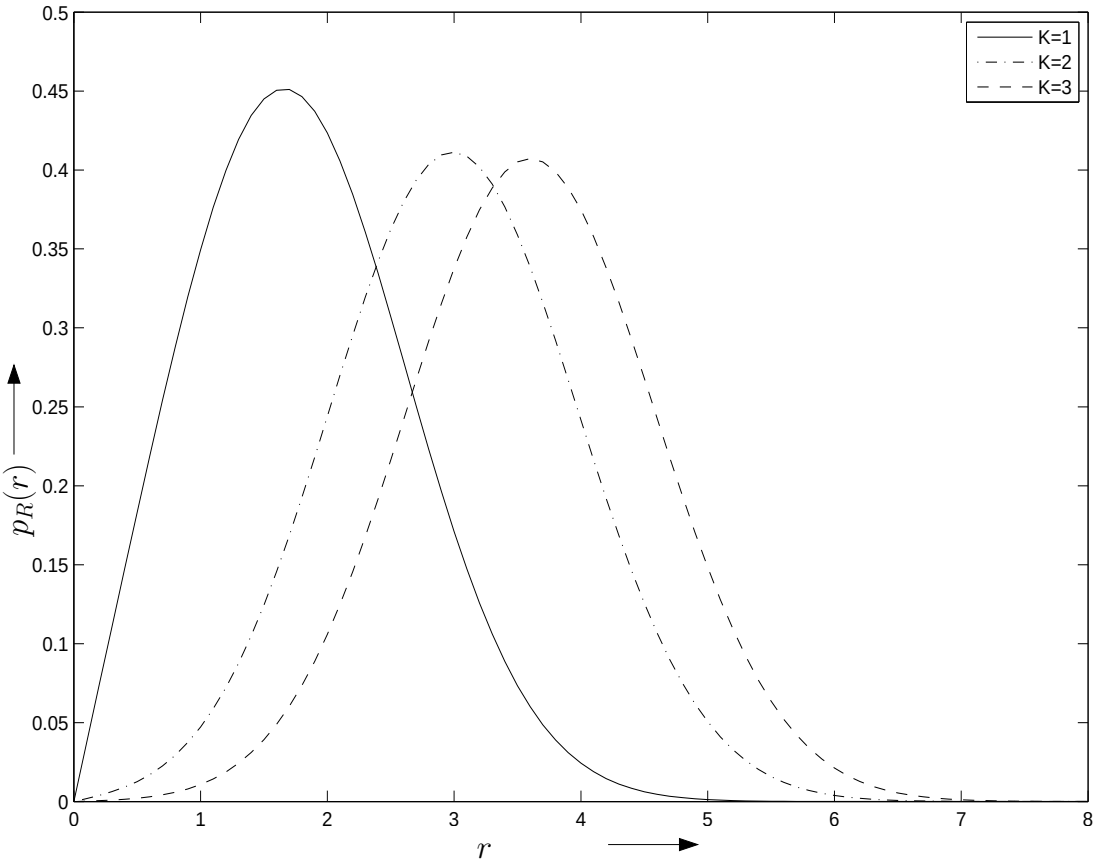

Figure 2.3: Sample Rice fading intensity pdfs

Let's define the Rice factor $K = s^2/2\sigma_r^2$, the ratio of the power of the dominant multipath component to the average fading power of the remaining, non-specular multipath [9]. The normalized pdf of (2.17) can be re-stated as

$$p_R(r) = 2(K+1)r \cdot \exp(-K-(K+1)r^2)\mathrm{I}_0(2r\sqrt{K(K+1)}) \qquad (2.18)$$

Notices that, when $K \longrightarrow 0$, the pdf becomes Rayleigh distribution. Figure 2.3 depicts the pdf of Rice distributions with different K values.

2.3 State-of-the-art of Hybrid RF/FSO Systems

In order to guarantee the connectivity of a data network, commonly link availability is required to meet some requirement for different deployment pro-

poses. For enterprise applications, link availability is required to be greater than 99%, called enterprise-class availability. For carrier or internet service providers (ISP), the availability needs to be greater than 99.999%. This is called carrier-class availability.

In comparison with other last mile technologies such as fiber optic, the main barrier for FSO deployment is that its availability is variable and difficult to predict due to weather. For example, fiber optic cable attenuates the transmission power at a constant, predictable rate. Current multi-mode fiber attenuates at 2 to 3 dB/km, and single-mode fiber attenuates at 0.2 to 0.5 dB/km. On the other hand, atmospheric attenuation can vary from 0.2 dB/km in clear weather to 250 dB/km in very heavy fog [10]. The large attenuation values in certain weather conditions can reduce the up-time or link availability of FSO systems.

The link availability can be used for link budget calculation. From Section 2.2 it is known that the large-scale attenuation depends on both the distance of the link and the weather conditions. Hence, for the same transmitted power, the trade off is between the link distance and the link availability. The maximum link distance for specific types of link availability requirements can be determined for system transmitted power and weather conditions. Reference [10] gives a detailed examination of the distance limitation of FSO systems for both carrier and enterprise applications. It is concluded from [10] that under some weather conditions such as heavy fog, the maximum link distance is only at the range of a few hundred meters, regardless of the value of the transmitted power or the size of the receive optics. To overcome this major drawback, the most cost-effective solution is to incorporate an RF back-up. The only weather condition which negatively affects both links is heavy rain and heavy fog simultaneously. However, this does not happen since rain droplets would absorb the suspended fog water droplets [14].

A great amount of research has been done on hybrid FSO/RF links [11, 12, 14, 15, 37, 38]. One is to use RF link as a complementary channel [11]. In this

scheme, data is sent exclusively through the FSO link until a drop of the link quality is observed. In this case, data will switch to the RF link completely. This requires the feedback of the link availability to the transmitter. Another scheme uses RF link as a redundant link [13]. Identical information is sent into both links. At the receiver, the data at the link with higher signal quality will be picked up. This does not require link condition knowledge before hand, with the trade-off of redundant data sent in both links. All these schemes proposed or used do not give consideration on utilizing the diversity of the two channels to maximize the capacity. Recently, a scheme proposed by Vangala et al. [37] utilizes hybrid channel codes to achieve a high efficiency and exploits diversity of FSO/RF channels. A hybrid channel code is the designed that a sequence first goes through a non-uniform encoder followed by a rate-adaptive code convertor. Non-uniform codes are used for data transmission over a set of parallel independent sub-channels [39]. In [37], a codeword of length n is generated by a single low-density parity check (LDPC) encoder. The codeword is then transmitted over the set of channels such that $n(j)$ bits in any codeword are transmitted over the jth channel. Additionally, in order to maintain an acceptable quality of service when channels are time-variant, Vangala et al. proposes to using punctured coded so that code rate is adaptive to channel conditions. However, Vangala et al. only provides the concept of his design, no actual code searching method and results are presented. Also, the proposed system is not robust to any weather conditions since feedback of the weather condition is required. In this thesis, we could propose a joint BICM scheme which splits each codeword accordingly into two bit streams and transmits them via both FSO/RF channels. A diversity is reached.

Table 2.1: Weather–dependent parameters of FSO and RF sub–systems [9, 40, 25, 26].

Weather conditions	a_1 [dB/km]	a_{rain} [dB/km]	C_n^2
Clear air	0.43	0	$5 \cdot 10^{-14}$
Haze	4.2	0	$1.7 \cdot 10^{-14}$
Light fog	20	0	$3 \cdot 10^{-15}$
Moderate fog	42.2	0	$2 \cdot 10^{-15}$
Heavy fog	125	0	$1 \cdot 10^{-15}$
Moderate rain (12.5 mm/h)	5.8	5.6	$5 \cdot 10^{-15}$
Heavy rain (25 mm/h)	9.2	10.2	$4 \cdot 10^{-15}$

Chapter 3

Hybrid FSO/RF System Model

In Chapter 2, we have described the channel fading models for FSO channel and RF channel, respectively. In this chapter, we derive the signal-to-noise ratio (SNR) for both channels separately based on the channel fading models detailed in Chapter 2, as well as the link budget calculation. The link budget calculation is dependent on weather condition and link distance. Here, we adopt the weather attenuation models and values of attenuation coefficient provided in Chapter 2. We later describe the transmitter and receiver structures of your system.

3.1 System Model

In this thesis, we assume that both the FSO and the RF sub–systems have one transmit and one receive aperture, respectively. Furthermore, we assume that both the FSO and RF channels are constant during one codeword. Because of the very high data rates considered, this is a reasonable assumption even for mobile hybrid RF/FSO systems [12, 38].

FSO Channel: We consider an FSO system with intensity modulation and direct detection (IM/DD) [6]. The photocurrent generated by the photodetector is integrated over one symbol interval and the constant bias due to background radiation is removed. Under these conditions, for high–energy,

shot noise (caused by background radiation) limited FSO systems the sufficient statistic in the k_1th symbol interval can be modeled as [27]–[40]

$$r_1[k_1] = P_1 g_1 h_1 \rho x_1[k_1] + n_1[k_1], \tag{3.1}$$

where P_1, g_1, h_1, ρ, $x_1[k_1] \in \mathcal{X}_1 \triangleq \{0, 2\}$ ($M_1 \triangleq |\mathcal{X}_1| = 2$), and $n_1[k_1]$ are the transmitted optical power, the average gain of the FSO link, the FSO fading gain with $\mathcal{E}\{h_1\} = 1$, the responsivity of the photodetector, the transmitted OOK symbol, and real–valued additive white Gaussian noise (AWGN) with variance $\sigma_1^2 \triangleq \mathcal{E}\{|n_1[k_1]|^2\}$, respectively. The Beers–Lambert Law dictates g_1. For the probability density function (pdf) $f_1(h_1)$ of h_1 we adopt the popular Gamma–Gamma fading model 2.6. Based on (3.1) we define the electrical SNR of the FSO link as

$$\gamma_1 \triangleq \frac{(\mathcal{E}\{P_1 g_1 h_1 \rho x_1[k_1]\})^2}{\sigma_1^2} = \frac{P_1^2 g_1^2 \rho^2}{\sigma_1^2}. \tag{3.2}$$

RF Channel: The received signal of the RF channel in the k_2th symbol interval is modeled as

$$r_2[k_2] = \sqrt{P_2}\sqrt{g_2} h_2 x_2[k_2] + n_2[k_2], \tag{3.3}$$

where P_2, g_2, h_2, $x_2[k_2] \in \mathcal{X}_2$, and $n_2[k_2]$ denote the RF transmit power, the average power gain of the RF link, the RF fading gain with $\mathcal{E}\{h_2^2\} = 1$, the modulated RF symbol with $\mathcal{E}\{|x_2[k_2]|^2\} = 1$ taken from M_2–ary symbol alphabet $\mathcal{X}_2$ (e.g. quadrature amplitude modulation (QAM)), and complex AWGN with variance $\sigma_2^2 \triangleq \mathcal{E}\{|n_2[k_2]|^2\}$, respectively. Assuming a carrier frequency of 60 GHz, the effective gain can be modeled as [9]

$$g_2\,[\text{dB}] \triangleq G_t + G_r - 20\log_{10}\left(\frac{4\pi L}{\lambda_2}\right) - a_{\text{oxy}} L - a_{\text{rain}} L, \tag{3.4}$$

where G_t and G_r denote the transmit and receive antenna gains, respectively, λ_2 is the wavelength of the RF system, and a_{oxy} and a_{rain} are the attenuations caused by oxygen absorbtion and rain (both in dB/km), respectively. The RF noise variance is given by $\sigma_2^2\,[\text{dB}] = BN_0 + N_F$, where B, N_0, and N_F denote

the RF bandwidth, the noise power spectral density (in dBm/MHz), and the noise figure of the receiver, respectively [9]. The fading gain h_2 can be modeled as Ricean distributed [4, 8, 9], where the Ricean factor K depends on various factors such as link distance, antenna height, and the environment, and may also change with time in mobile applications [12, 38, 41]. The SNR of the RF link is defined as

$$\gamma_2 \triangleq \frac{\mathcal{E}\{|\sqrt{P_2 g_2} h_2 x_2[k_1]|^2\}}{\sigma_2^2} = \frac{P_2 g_2}{\sigma_2^2}. \tag{3.5}$$

Since both a_1 and a_{rain} are weather dependent cf. Chapter 2, we show the SNRs γ_1 and γ_2 in Fig. 3.1 for different weather conditions, where we have adopted $P_1 = P_2 = 10$ mW and the values given in Tables 3.1 and 2.1 for all relevant parameters of the FSO and RF sub–systems. The values in Tables 3.1 and 2.1 were taken from [8, 9, 23, 40, 25, 26]. The values for a_1 and a_{rain} are summary of those stated in Section 2.1.2 and Section 2.2.3

3.2 Transmitter Structure

The transmitter structure of the proposed hybrid RF/FSO system is shown in the top part of Fig. 3.2. A sequence of K_c information bits $\boldsymbol{b} \triangleq [b[1]\ b[2]\ \ldots\ b[K_c]$ is encoded with a convolutional encoder (CC) of rate R_c to produce the coded sequence $\boldsymbol{c} \triangleq [c[1]\ c[2]\ \ldots\ c[N_c]]$ of length $N_c \triangleq K_c/R_c$. Subsequently, $\boldsymbol{c}$ is divided into two sub–sequences, $\boldsymbol{c}_1$ and $\boldsymbol{c}_2$, according to assignment pattern (AP) $\boldsymbol{a} \triangleq \{0, 1\}^N$, which contains n_1 "1"s and $n_2 = N - n_1$ "0"s. For this purpose $\boldsymbol{c}$ is grouped into blocks of N bits and within each block bits in positions where $\boldsymbol{a}$ has a "1" are assigned to $\boldsymbol{c}_1$, while bits in positions where $\boldsymbol{a}$ has a "0" are assigned to $\boldsymbol{c}_2$. Thus, $\boldsymbol{c}_1$ and $\boldsymbol{c}_2$ are sequences of lengths $n_1 N_c/N$ and $n_2 N_c/N$, respectively. The bits in $\boldsymbol{c}_1$ and $\boldsymbol{c}_2$ are interleaved with interleavers Π_1 and Π_2, respectively, and the interleaved bit sequences are mapped to symbols $x_1[k_1]$ and $x_2[k_2]$ using Gray labeling, respectively.[1] The symbol rates of

[1]We note that since binary modulation is used over the FSO link, interleaver Π_1 is not needed for the considered channel model. However, we have included Π_1 since, in practice,

Table 3.1: Parameters of FSO and RF sub–systems [8, 9, 23, 40].

FSO System		
Parameter	Symbol	Value
Wavelength	λ_1	1550 nm
Symbol rate	$1/T_1$	1 Gbit/s
Responsivity	ρ	$0.5\,\frac{1}{\mathrm{V}}$
Noise variance	σ_1^2	$10^{-14}\,\mathrm{A}^2$
RF System		
Parameter	Symbol	Value
Carrier frequency	f_c	60 GHz
Bandwidth	B	250 MHz
Symbol rate	$1/T_2$	250 Msym/s
Transmit antenna gain	G_t	44 dBi
Receive antenna gain	G_r	44 dBi
Attenuation (Oxygen)	a_{oxy}	15.1 dB/km
Ricean factor	K	6 dB
Noise power spectral density	N_0	-114 dBm/MHz
Receiver noise figure	N_F	5 dB

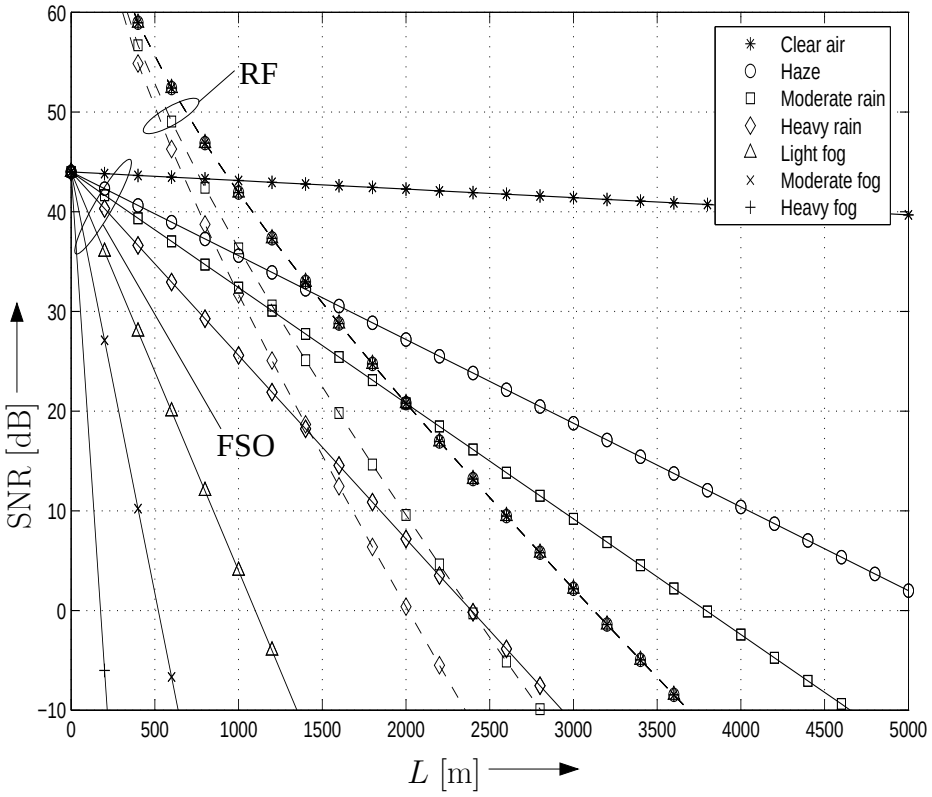

Figure 3.1: SNR of FSO (γ_1) and RF (γ_2) systems vs. link distance L for transmit powers of $P_1 = P_2 = 10$ mW and different weather conditions. The values for a_1 and a_{rain} have been taken from Table 2.1. All other link parameters have been chosen as in Table 3.1.

both sub–systems are given by

$$\frac{1}{T_\nu} \triangleq \frac{n_\nu}{\log_2(M_\nu) R_c N T_b} \left[\frac{\text{symbols}}{s}\right], \qquad \nu \in \{1, 2\}, \tag{3.6}$$

where T_1 and T_2 denote the symbol durations of the FSO and the RF sub–systems, respectively, and $1/T_b$ is the information bit rate. Therefore, assuming FSO and RF sub–channels with coded bit rates of $1/T_1$ and $\log_2(M_2)/T_2$, respectively, n_1 and n_2 have to fullfill

$$\frac{n_1}{n_2} = \frac{T_2}{\log_2(M_2) T_1}. \tag{3.7}$$

burst errors may be caused by e.g. bird fly–through in the FSO link. In this case, the interleaver would be beneficial.

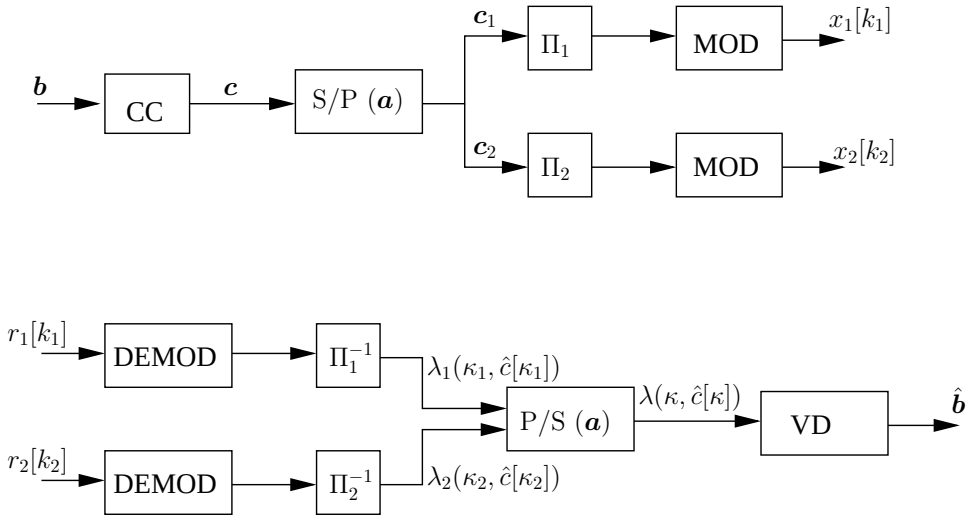

Figure 3.2: Transmitter and receiver structure of proposed hybrid RF/FSO system. S/P: Serial–to–parallel conversion. P/S: Parallel–to–serial conversion. VD: Viterbi decoder.

We note that both the CC and the AP $\boldsymbol{a}$ have to be optimized for maximum performance, cf. Sections 4 and 5.

3.3 Receiver Structure

To simplify our notation, we define the normalized received signals $r'_\nu[k_\nu] \triangleq r_\nu[k_\nu]/\sigma_\nu$. As shown in the bottom part of Fig. 3.2, the received symbol streams of both links are demodulated to obtain the bit metrics [19]

$$\lambda_\nu(\kappa'_\nu, \hat{c}[\kappa'_\nu]) \triangleq \min_{x_\nu \in \mathcal{X}^i_\nu(\hat{c}[\kappa'_\nu])} \{\xi_\nu |r'_\nu[k_\nu] - \sqrt{\gamma_\nu} h_\nu x_\nu|^2\}, \qquad \nu \in \{1, 2\}, \tag{3.8}$$

where $\mathcal{X}^i_\nu(c)$ denotes the subset of all symbols $x_\nu \in \mathcal{X}_\nu$ whose label has the value $c \in \{0, 1\}$ in position i, $1 \le i \le \log_2 M_\nu$, $\xi_1 \triangleq 1/2$ and $\xi_2 \triangleq 1$ account for the fact that $n_1[k_1]$ and $n_2[k_2]$ are real and complex AWGN, respectively, and κ'_ν is determined by k_ν and i. The bit metrics are deinterleaved with Π_1^{-1} and Π_2^{-1}, respectively, and parallel–to–serial converted based on AP $\boldsymbol{a}$ to produce a single sequence of bit metrics $\lambda(\kappa, \hat{c}[\kappa])$, $1 \le \kappa \le N_c$, corresponding to the coded sequence $\boldsymbol{c}$. Finally, a standard Viterbi decoder (VD) is used to generate an estimate $\hat{\boldsymbol{b}}$ for the transmitted bit sequence based on these bit metrics.

Chapter 4

Performance Analysis and System Optimization

4.1 Asymptotic Pairwise Error Probability

For calculation of the union bound on the CEP, the PEP is needed. Consider an error event of length d, where d_1 erroneous bits correspond to symbols $x_1[k_{1,i}] \in \mathcal{X}_1$, $1 \leq i \leq d_1$, transmitted over the FSO link and $d_2 \triangleq d - d_1$ bits correspond to symbols $x_2[k_{2,i}] \in \mathcal{X}_2$, $1 \leq i \leq d_2$, transmitted over the RF link. The corresponding metric difference can be expressed as [19]

$$\begin{aligned}\Delta &= \frac{1}{2}\sum_{i=1}^{d_1}\left(|r_1'[k_{1,i}] - \sqrt{\gamma_1}h_1\bar{x}_1[k_{1,i}]|^2 - |r_1'[k_{1,i}] - \sqrt{\gamma_1}h_1x_1[k_{1,i}]|^2\right) \\ &\quad + \sum_{i=1}^{d_2}\left(|r_2'[k_{2,i}] - \sqrt{\gamma_2}h_2\bar{x}_2[k_{2,i}]|^2 - |r_2'[k_{2,i}] - \sqrt{\gamma_2}h_2x_2[k_{2,i}]|^2\right), \quad (4.1)\end{aligned}$$

where $x_\nu[k_{\nu,i}] \neq \bar{x}_\nu[k_{\nu,i}] \in \mathcal{X}_\nu$, $\nu \in \{1, 2\}$. Based on (4.1) the conditional PEP can be obtained as

$$P_e(\boldsymbol{x} \to \bar{\boldsymbol{x}}|h_1, h_2) \triangleq \Pr\{\Delta < 0\} = Q\left(\sqrt{\gamma_1 h_1^2 d_1 + \gamma_2 h_2^2 d_2^2(\boldsymbol{x}, \bar{\boldsymbol{x}})/2}\right), \quad (4.2)$$

where vectors $\boldsymbol{x}$ and $\bar{\boldsymbol{x}}$ contain the involved $x_\nu[k_{\nu,i}]$ and $\bar{x}_\nu[k_{\nu,i}]$, respectively, and

$$d_2^2(\boldsymbol{x}, \bar{\boldsymbol{x}}) \triangleq \sum_{i=1}^{d_2} |x_2[k_{2,i}] - \bar{x}_2[k_{2,i}]|^2 \quad (4.3)$$

While the exact average PEP can be expressed as

$$P_e(\boldsymbol{x} \to \bar{\boldsymbol{x}}) \triangleq \mathcal{E}_{h_1,h_2}\{P_e(\boldsymbol{x} \to \bar{\boldsymbol{x}}|h_1, h_2)\} \tag{4.4}$$

, and cannot be calculated in closed form, we derive the average PEP for asymptotic case ($\gamma_1 \gg 1$ and $\gamma_2 \gg 1$).

First by using the modified version of the Gaussian Q–function

$$Q(x) = \frac{1}{\pi}\int_0^{\pi/2} e^{-x^2/(2\sin^2\theta)}\,\mathrm{d}\theta \tag{4.5}$$

and (4.2), the average PEP can be expressed as

$$P_e(\boldsymbol{x} \to \bar{\boldsymbol{x}}) = \frac{1}{\pi}\int_0^{\pi/2} I_1(\theta)\, I_2(\theta)\,\mathrm{d}\theta, \tag{4.6}$$

where

$$I_1(\theta) \triangleq \mathcal{E}_{h_1}\{\exp(-\gamma_1 h_1^2 d_1^2/(2\sin^2\theta))\} \tag{4.7}$$

and

$$I_2(\theta) \triangleq \mathcal{E}_{h_2}\{\exp(-\gamma_2 h_2^2 d_2^2(\boldsymbol{x}, \bar{\boldsymbol{x}})/(4\sin^2\theta))\} \tag{4.8}$$

To arrive at a closed–form solution, we concentrate on the high SNR regime ($\gamma_1 \gg 1$ and $\gamma_2 \gg 1$). In this case, it has been shown in [42, 24] that the pdf $f_\nu(h_\nu)$ may be replaced by the first term of its Taylor series expansion

$$f_\nu(h_\nu) = m_\nu h_\nu^{l_\nu} + o(h_\nu^{l_\nu}), \quad h_\nu \geq 0, \qquad \nu \in \{1, 2\}, \tag{4.9}$$

where $m_1 \triangleq (\alpha\beta)^\beta\Gamma(\alpha-\beta)/[\Gamma(\alpha)\Gamma(\beta)]$, $l_1 \triangleq \beta - 1$, $\alpha > \beta$, $\alpha - \beta \neq \mathbb{Z}$ for Gamma–Gamma fading [24] and $m_2 \triangleq 2(1+K)e^{-K}$, $l_2 \triangleq 1$ for Ricean fading [42]. We note that the conditions $\alpha > \beta$ and $\alpha - \beta \neq \mathbb{Z}$ are valid in practice, cf. (2.7), (2.8), [7]. Exploiting (4.9) and the integral

$$\int_0^\infty x^{m-1}\exp(-sx^2)\,\mathrm{d}x = s^{-m/2}\Gamma(m/2) \tag{4.10}$$

for $m > 0$, $s > 0$ [43, Eq. (3.4782)], For $I_1(\theta)$ we obtain

$$I_1(\theta) = \int_0^\infty \exp\left(-\frac{\gamma_1 d_1 h^2}{2\sin^2\theta}\right) m_1 h^{\beta-1}\mathrm{d}h \tag{4.11}$$

Let $u = \frac{h}{\sin\theta}$, 4.11 becomes

$$\begin{aligned} I_1(\theta) &= m_1 \int_0^\infty \exp\left(-\frac{\gamma_1 d_1 u^2}{2}\right) u^{\beta-1} \sin^{\beta-1}\theta \mathrm{d}u \\ &= \frac{2^{\beta/2} m_1 \Gamma(\beta/2)}{\gamma_1^{\beta/2} d_1^{\beta/2}} \sin^\beta \theta \end{aligned} \tag{4.12}$$

For $I_2(\theta)$ we obtain

$$I_2(\theta) = \int_0^\infty \exp\left(-\frac{\gamma_2 d_2 h^2}{4\sin^2\theta}\right) m_2 h \mathrm{d}h \tag{4.13}$$

Let $u = \frac{h}{\sin\theta}$, 4.13 becomes

$$\begin{aligned} I_2(\theta) &= m_2 \sin\theta \int_0^\infty \exp\{\frac{\gamma_2 d_2^2(\boldsymbol{x}, \bar{\boldsymbol{x}}) u^2}{4}\} \mathrm{d}u \\ &= \frac{4 m_2}{\gamma_2 d_2^2(\boldsymbol{x}, \bar{\boldsymbol{x}})} \sin^2\theta. \end{aligned} \tag{4.14}$$

Combining (4.6) with (4.12) and (4.14) and exploiting

$$\int_0^{\pi/2} \sin^{m-1} x \, \mathrm{d}x = \Gamma(1/2)\Gamma(m/2)/[2\Gamma((m+1)/2)] \tag{4.15}$$

[43, Eq. (3.6211)] leads to

$$P_e(\boldsymbol{x} \to \bar{\boldsymbol{x}}) \doteq \frac{C}{\gamma_1^{\beta/2}\gamma_2} \cdot \frac{1}{d_1^{\beta/2} d_2^2(\boldsymbol{x}, \bar{\boldsymbol{x}})} \dot{\leq} \frac{C}{d_{\min}^2 \gamma_1^{\beta/2}\gamma_2} \cdot \frac{1}{d_1^{\beta/2} d_2}, \tag{4.16}$$

where

$$C \triangleq \frac{2^{\beta/2+2}(1+K)e^{-K}(\alpha\beta)^\beta \Gamma(\alpha-\beta)\Gamma(\beta/2)\Gamma(\beta/2+3/2)}{[\sqrt{\pi}\Gamma(\alpha)\Gamma(\beta)\Gamma(\beta/2+2)]}, \tag{4.17}$$

$d_{\min}$ denotes the minimum Euclidean distance of $\boldsymbol{\mathcal{X}}_2$, and $d_1 > 0$ and $d_2 > 0$ were assumed for derivation of (4.16). We also exploited the inequality $d_2^2(\boldsymbol{x}, \bar{\boldsymbol{x}}) \geq d_{\min}^2 d_2$ in (4.16). Eq. (4.16) shows that codes with $d_1 > 0$ and $d_2 > 0$ guarantee that the asymptotic PEP decreases with increasing SNRs γ_1 and γ_2. In this case, the RF and the FSO sub–systems both contribute to the reliability of the transmission and diversity is achieved. Thus, in this thesis, we will only consider codes which achieve $d_1 > 0$ and $d_2 > 0$. We note that Fig. 3.1 shows

that in practice it might not be possible to simultaneously achieve $\gamma_1 \gg 1$ and $\gamma_2 \gg 1$, which was assumed for derivation of (4.16), under all weather conditions and for all link distances. Nevertheless, codes guaranteeing $d_1 > 0$ and $d_2 > 0$ are robust against low SNR in one sub–channel and are able to exploit the high SNR in the other sub–channel.

4.2 Asymptotic Codeword Error Probability

From (4.16) we can obtain an upper bound on the asymptotic CEP as [22]

$$P_w \stackrel{\cdot}{\leq} \frac{C\,F}{d_{\min}^2 \gamma_1^{\beta/2} \gamma_2} \tag{4.18}$$

$$F \triangleq \sum_{d_1} \sum_{d_2} \frac{w(d_1, d_2)}{d_1^{\beta/2} d_2} \tag{4.19}$$

where $w(d_1, d_2)$ denotes the number of error events with Hamming distances d_1 and d_2 for the FSO and RF sub–channels, respectively. For the considered problem $w(d_1, d_2)$ depends on both the CC *and* the AP $\boldsymbol{a}$. $w(d_1, d_2)$ is given by the coefficients of the generalized transfer function (GTF) [21, 22]

$$T(D_1, D_2) = \sum_{d_1} \sum_{d_2} w(d_1, d_2) D_1^{d_1} D_2^{d_2}. \tag{4.20}$$

We will explain in Section 5 how $T(D_1, D_2)$ can be efficiently computed for the problem at hand. It is well known that the union bound in (4.18) is not necessarily tight. However, despite this deficiency, it was found in [22] that for homogeneous block fading channels codes optimized according to the union bound still outperform codes optimized according to other criteria [17, 18]. Therefore, in Chapter 5, we will introduce a CC and AP search procedure which is based on (4.18).

4.3 Transmit Power Assignment

The total transmit power is given by $P_t = P_1 + P_2$ and should be divided in an optimal way between P_1 and P_2. Furthermore, in practice, the maximum

FSO transmit power $P_{1,\max}$ and the maximum RF transmit power $P_{2,\max}$ are both limited [3, 44]. From (3.2), (3.5), and (4.18) we observe that the upper bound on P_w is proportional to $1/(P_1^{\beta}P_2)$. Since our goal is the minimization of the upper bound on P_w, we obtain the following optimization problem:

$$\min_{P_1,P_2} \quad P_1^{-\beta}P_2^{-1} \tag{4.21}$$

$$\text{s.t.} \quad 0 \le P_1 \le P_{1,\max} \tag{4.22}$$

$$0 \le P_2 \le P_{2,\max} \tag{4.23}$$

$$P_1 + P_2 \le P_t \tag{4.24}$$

The optimum values for P_1 and P_2 can be found with the standard Karush–Kuhn–Tucker approach [45] for constraint optimization problems. Assuming there is a feasible solution, i.e., $P_t \le P_{1,\max} + P_{2,\max}$, the optimum power assignment is given by

$$\begin{aligned}
&P_1 = \tfrac{\beta}{1+\beta}P_t,\ P_2 = \tfrac{1}{1+\beta}P_t, && \text{if } P_t \le \min\left\{\tfrac{1+\beta}{\beta}P_{1,\max},\ (1+\beta)P_{2,\max}\right\} \\
&P_1 = P_{1,\max},\ P_2 = P_t - P_{1,\max}, && \text{if } \tfrac{1+\beta}{\beta}P_{1,\max} < P_t \le (1+\beta)P_{2,\max} \\
&P_1 = P_t - P_{2,\max},\ P_2 = P_{2,\max}, && \text{if } (1+\beta)P_{2,\max} < P_t \le \tfrac{1+\beta}{\beta}P_{1,\max}
\end{aligned} \tag{4.25}$$

For the case $P_t \le \min\{(1+1/\beta)P_{1,\max},\ (1+\beta)P_{2,\max},\ P_{1,\max}+P_{2,\max}\}$ it is interesting to compare the optimum power assignment according to (4.25) with the pragmatic assignment $P_1 = P_2 = P_t/2$. From (4.18) and (4.25) we observe that the asymptotic power gain achievable with the optimum power assignment is

$$G_P(\beta) = 2\frac{\beta^{\frac{\beta}{1+\beta}}}{1+\beta}. \tag{4.26}$$

Not surprisingly, for $\beta = 1$ (4.26) yields $G_P(1) = 1$ since in this case equal power assignment is optimum, cf. (4.25). For $\beta = 2$, $\beta = 5$, and $\beta = 10$ we obtain from (4.26) power gains of 0.24 dB, 1.15 dB, and 1.69 dB, respectively. Furthermore, it can be shown that $G_P(\beta) \le 2$, $\forall\beta > 0$, i.e., the maximum power gain is limited to 3 dB, where the maximum gain is achieved for $\beta \to 0$ and $\beta \to \infty$. It is interesting to note that provided $d_1 > 0$ and $d_2 > 0$ the optimum power assignment is independent of the CC and the AP but only depends on the statistics of the FSO channel.

4.4 Bound on R_c

For the CC and AP search it is of interest to find a bound on R_c that guarantees that codes with $d_1 > 0$ and $d_2 > 0$ can be found. In this context, we note that the overall code rate including the effect of $\boldsymbol{a}$ is $R_\nu \triangleq NR_c/n_\nu$ for sub–channel $\nu \in \{1, 2\}$. It is clear that $d_\nu > 0$ can only be achieved if $R_\nu \leq 1$ [29]. Thus, we obtain the necessary condition

$$R_c \leq R_{c,\max} \triangleq \min_{\nu\in\{1,2\}} \left\{\frac{n_\nu}{N}\right\} = \min_{\xi\in\{n_1/n_2,\, n_2/n_1\}} \left\{\frac{1}{1+\xi}\right\}. \tag{4.27}$$

A simple code with $R_c = R_{c,\max}$ that achieves $d_\nu > 0$, $\nu \in \{1, 2\}$, is the repetition code with an arbitrary AP having n_1 "1"s and n_2 "0"s . Thus, (4.27) is sufficient and necessary for the existence of a full diversity code (i.e., $d_\nu > 0$, $\nu \in \{1, 2\}$). Note that by exploiting (3.7) $R_{c,\max}$ may equivalently be formulated in terms of T_1, T_2, and $\log_2(M_2)$.

If both the FSO and the RF sub–channels support the same coded bit rate, $n_1/n_2 = 1$ follows from (3.7), and we obtain from (4.27) $R_c \leq 1/2$. If the FSO and RF sub–channels support different coded bit rates, i.e., $n_1/n_2 \neq 1$, the maximum code rate $R_{c,\max}$ is lower than 1/2.

Chapter 5

Code and Assignment Pattern Search

In this chapter, we explain the proposed CC and AP search procedure. Furthermore, we outline how the GTF is computed and present some CC and AP search results.

5.1 Search Algorithm

Since we adopt the upper bound on the CEP in (4.18) as optimality criterion, the optimum CC and AP have to minimize F in (4.19). To limit the complexity of the search procedure and following the reasoning in [22] we limit d_1 and d_2 in the sums in (4.19) to $d_1 + d_2 \leq 2d_f - 1$, where d_f is the free distance of the code. We assume that parameters T_1, T_2, and M_2 of the hybrid RF/FSO system are given. For the proposed CC and AP search we first have to select the desired constraint length q and rate $R_c = k_c/n_c \leq R_{c,\max}$ (k_c and n_c are integers) of the CC and the length N of the AP. Subsequently, we generate all possible CCs with the prescribed q and R_c and all possible APs meeting (4.27). For all possible combinations of the generated CCs and APs we calculate the corresponding F, and retain that combination of code and AP as the optimum one which has the minimum F.

Now, some remarks on how to choose q and N are in order. The decoding complexity is only affected by q but not by N. Larger q will generally yield a better performance at the expense of a higher decoding complexity. The complexity of the proposed exhaustive search procedure increases with both q and N. For larger q there are more generator polynomials to be examined and for larger N there are more possible APs for each combination of n_1 and n_2. On the other hand, since larger N provide more flexibility in choosing the AP, larger N generally yield a superior performance as compared to smaller N.

5.2 Computation Method

In the proposed search procedure, F has to be calculated for each considered combination of CC and AP. Therefore, the GTF $T(D_1, D_2)$ has to be computed for each combination of CC and AP. For simplicity, we assume ideal interleavers and neglect any edge effects caused by finite length codewords. As mentioned before, the coefficients $w(d_1, d_2)$ of the GTF denote the number of error events with Hamming distances d_1 and d_2 in the FSO and RF sub–channels, respectively. Without loss of generality, we may assume that an all–zero sequence was transmitted and the decoded codeword constitutes the corresponding error event. Thus, $w(d_1, d_2)$ is the number of codewords $\boldsymbol{c}_1$ and $\boldsymbol{c}_2$ with weights d_1 and d_2, respectively. Based on this observation, we can efficiently compute $T(D_1, D_2)$ with the approach proposed in [22].

For this purpose, we consider the trellis diagram of a CC with rate $R_c = k_c/n_c$ and 2^q states S_j, $1 \leq j \leq 2^q$, with S_1 being the all–zero state. For the tth trellis segment we define the elements A_{ij} of $2^q \times 2^q$ matrix $\boldsymbol{A}_t(D_1, D_2)$ as follows [22, 46]. If a trellis branch connects state S_i with state S_j, $A_{ij} = D_1^{w_1} D_2^{w_2}$ where w_1 and w_2 denote the number of "1"s assigned to $\boldsymbol{c}_1$ and $\boldsymbol{c}_2$ in the considered trellis segment according to the AP, respectively. If states S_i and S_j are not connected by a trellis branch, $A_{ij} = 0$. Considering a codeword of length $T \triangleq T_0 \cdot \mathrm{lcm}(n_c, N)$, where T_0 is an integer and $\mathrm{lcm}(n_c, N)$ is the lowest

common multiple of n_c and N, the GTF can be obtained as [46, 22]

$$T(D_1, D_2) = A_{11}(D_1, D_2) - 1, \tag{5.1}$$

where $A_{11}(D_1, D_2)$ is the first element of the first column of matrix

$$\boldsymbol{A}(D_1, D_2) \triangleq \prod_{t=1}^{T} \boldsymbol{A}_t(D_1, D_2) = \left(\prod_{t=1}^{\mathrm{lcm}(n_c, N)} \boldsymbol{A}_t(D_1, D_2) \right)^{T_0}. \tag{5.2}$$

In (5.2), we have exploited the fact that the CC trellis including the effect of the AP is periodic with period $\mathrm{lcm}(n_c, N)$. Based on (5.1) and (5.2) the weights $w(d_1, d_2)$, $d_1 + d_2 \leq 2d_f - 1$, can be efficiently computed using standard software such as MATLAB$^{\mathrm{TM}}$.

5.3 CC and AP Search Results

A few example CCs and APs found with the proposed search method are provided in Table 5.1 for RF channels with 16–QAM ($R_c = 1/2$ and $1/4$) and 4–QAM ($R_c = 1/3$), respectively. These codes were optimized for $K = 6$ dB and $\alpha = 2.5$ and $\beta = 2$, which are valid for haze and $L = 3.5$ km. We note that the optimum CCs and APs are not very sensitive to the exact values of K, α, and β. Thus, we employed the codes provided in Table 5.1 for all simulation results presented in Section 7. We also provide the free distance d_f and the resulting value for F, cf. (4.19), in Table 5.1. For each code in Table 5.1 two different AP lengths N are considered. As expected, the larger N generally leads to a smaller F, and thus better performance, due to the larger flexibility in assigning the coded bits to the sub–channels. However, for the considered examples the potential gains by using the larger N are comparatively small.

Table 5.1: Convolutional codes and assignment patterns optimized for $\alpha = 2.5$, $\beta = 2$, and $K = 6$ dB. The generator polynomials $\boldsymbol{g}$ and the assignment patterns are both in octal representation.

$R_c = 1/2$ and 16–QAM					
q	$\boldsymbol{g}$	N	$\boldsymbol{a}$	d_f	F
3	$(5, 7)$	4	(21)	5	58.0
3	$(5, 7)$	6	(46)	5	55.1
4	$(15, 17)$	4	(30)	6	105.0
4	$(15, 17)$	6	(51)	6	93.2
5	$(43, 35)$	4	(22)	7	170.0
5	$(43, 35)$	6	(62)	7	162.8
6	$(53, 75)$	4	(50)	8	368.3
6	$(53, 75)$	6	(52)	8	346.5
7	$(133, 171)$	4	(41)	10	3274.8
7	$(133, 171)$	6	(25)	10	3047.2
$R_c = 1/4$ and 16–QAM					
q	$\boldsymbol{g}$	N	$\boldsymbol{a}$	d_f	F
3	$(5, 7, 7, 7)$	8	(306)	10	31.0
3	$(5, 7, 7, 7)$	12	(3306)	10	29.8
4	$(13, 15, 15, 17)$	8	(230)	13	41.9
4	$(13, 15, 15, 17)$	12	(6314)	13	39.8
$R_c = 1/3$ and 4–QAM					
q	$\boldsymbol{g}$	N	$\boldsymbol{a}$	d_f	F
3	$(5, 7, 7)$	3	(3)	8	66.6
3	$(5, 7, 7)$	6	(53)	8	59.8
4	$(13, 15, 17)$	6	(55)	10	92.3
4	$(13, 15, 17)$	9	(665)	10	87.8
5	$(25, 33, 37)$	15	(33535)	12	214.2
6	$(47, 53, 75)$	15	(76266)	13	242.0

Chapter 6

Cut-off Rate Analysis

Since the cut–off rate constitutes the ultimate performance limit for convolutionally coded systems [29], in this section, we evaluate the cut–off rate of the proposed hybrid RF/FSO system. To simplify the derivation, we assume random APs assigning on average n_1 and n_2 bits to the FSO and RF channels, respectively. For simplicity of notation, we drop time indices k_1 and k_2 in this section. Taking also into account the bit interleaver, we have $1+\log_2(M_2)$ statistically independent parallel channels [19] for which the cut–off rate $R_0(h_1, h_2)$ for given channel gains h_1 and h_2 can be obtained as [47]

$$R_0(h_1, h_2) = (R_{1,\max} + R_{2,\max})[1 - \log_2(1 + B(h_1, h_2))] \,[\text{bit/s}], \tag{6.1}$$

where $R_{1,\max} \triangleq 1/T_1$, $R_{2,\max} \triangleq \log_2(M_2)/T_2$, and

$$B(h_1, h_2) \triangleq \frac{n_1}{N} B_1(h_1) + \frac{n_2}{N} B_2(h_2) \tag{6.2}$$

with

$$B_1(h_1) \triangleq \mathcal{E}_{r_1,c}\left\{\sqrt{p_1(r_1|x_1 = \bar{c}, h_1)/p_1(r_1|x_1 = c, h_1)}\right\} = \exp\left(-h_1^2 r_1/2\right), \tag{6.3}$$

$$B_2(h_2) \triangleq \sum_{i=1}^{\log_2(M_2)} \frac{B_{2,i}(h_2)}{\log_2(M_2)}, \tag{6.4}$$

, and

$$B_{2,i}(h_2) \triangleq \mathcal{E}_{r_2,c}\left\{\sqrt{\left(\sum_{x_2\in\mathcal{X}_2^i(\bar{c})} p_2(r_2|x_2,h_2)\right) / \left(\sum_{x_2\in\mathcal{X}_2^i(c)} p_2(r_2|x_2,h_2)\right)}\right\} \text{ [19].} \tag{6.5}$$

Here, $c \in \{0,1\}$, $\bar{c}$ denotes the complement of c, and $p_1(r_1|x_1,h_1)$ and $p_2(r_2|x_2,h_2)$ are the conditional pdfs of received signals r_1 and r_2, respectively. We note that the Bhattacharyya factors $B_1(h_1)$ and $B_{2,i}(h_2)$, $1 \le i \le \log_2(M_2)$, can be efficiently computed via Monte–Carlo simulation.

For comparison, the cut–off rates of the FSO and RF links are given by

$$R_{0,1}(h_1) = R_{1,\max}[1 - \log_2(1 + B_1(h_1))] \quad \text{[bit/s]}. \tag{6.6}$$

and

$$R_{0,2}(h_2) = R_{2,\max}[1 - \log_2(1 + B_2(h_2))] \quad \text{[bit/s]}. \tag{6.7}$$

respectively. Thus, a system which knows the sub–channel SNRs at the transmitter and performs independent BICM over both channels can achieve a cut–off rate of

$$R_{0,\mathrm{SNR}}(h_1,h_2) = R_{0,1}(h_1) + R_{0,2}(h_2). \tag{6.8}$$

Note that the sub–channel SNRs are weather dependent and do not have to be known if the proposed hybrid RF/FSO structure is adopted. This advantage over a system which knows the sub–channel SNRs comes at the expense of some potential performance degradation. In particular, assuming identical power assignment in both cases the inequality $R_0(h_1,h_2) \le R_{0,\mathrm{SNR}}(h_1,h_2)$ can be established by exploiting the convexity of the logarithm, $\log_2(1+B(h_1,h_2)) \ge n_1\log_2(1+B_1(h_1))/N + n_2\log_2(1+B_2(h_2))/N$, and (3.6) and (6.1)–(6.8). On the other hand, the rate of a system which does not know the SNR at the transmitter but performs independent BICM over both sub–channels is limited by

$$R_{0,\mathrm{ind}}(h_1,h_2) = 2\,\min\{R_{0,1}(h_1), R_{0,2}(h_2)\}, \tag{6.9}$$

since such a system has to assign the same rates to both sub–channels, and thus, will be limited by the weaker sub–channel.

Since we consider a block fading channel, it is of interest to define the outage probability

$$P_{\text{out}} = \Pr\{R_0(h_1, h_2) < R_{\text{target}}\}, \tag{6.10}$$

i.e., the probability that the considered system cannot support a rate of R_{target}. The outage probabilities for systems with independent BICM over both sub–channels with known and unknown sub–channel SNR at the transmitter are defined analogously to (6.10).

Chapter 7

Simulation Results

In this section, we study the performance of the proposed hybrid RF/FSO system with joint BICM over both links under various weather conditions. As performance measures we consider the outage probability as defined in Section 6 and the frame error rate (FER). The adopted values for the various system and channel parameters are given in Tables 3.1 and 2.1.

7.1 Outage Probability

In this subsection, we adopt 16–QAM for the RF link, i.e., the coded bit rate of both sub–channels is $R_{1,\max} = R_{2,\max} = 1$ Gbit/s, cf. Table 3.1. Figs. 7.1 and 7.2 show the outage probability as a function of the transmit power P_t for the proposed hybrid RF/FSO system with joint BICM over both sub–channels for target rates of $R_{\text{target}} = 1$ Gbit/s and $R_{\text{target}} = 500$ Mbit/s, respectively. Performance under clear air, haze, and moderate rain are considered for a link distance of $L = 2.5$ km. For comparison, the outage probabilities for hybrid RF/FSO systems performing independent BICM over both sub–channels are also shown in the presence and absence of CSI in form of the sub–channel SNRs at the transmitter, respectively. The corresponding cut–off rates are given in (6.8) and (6.9), respectively. For all considered schemes equal power assignment to the RF and FSO sub–channels is assumed. Since with de-

creasing visibility the FSO link attenuation increases while the severity of the fading decreases, cf. Table 2.1, for all considered schemes clear air yields the best performance for small P_t but haze results in a better performance for larger P_t due to the steeper slope of the outage curves. For all considered weather conditions independent BICM without CSI performs relatively poorly as performance is limited by the weaker sub–channel. Independent BICM with known CSI yields the best performance since the rates of both sub–channels can be perfectly adapted to the channel conditions. However, the proposed joint BICM scheme, which does not require CSI at the transmitter, achieves an excellent performance, especially for $R_{\text{target}} = 500$ Mbit/s, where the loss compared to independent BICM with CSI is negligible in the considered range of outage probabilities. The improved robustness of joint BICM for lower target rates is due to the stronger channel codes that can be used in this case, which provide better protection against low SNRs in one sub–channel.

7.2 Frame Error Rate (FER)

Throughout this section we assume that a frame contains 200 information bits. Besides the proposed joint BICM scheme we also show results for repetition coding over both channels with selection diversity at the receiver (RC–SD) as proposed in [13]. In RC–SD the same data is sent over both links and the receiver selects that frame which is deemed more reliable. For simplicity, we assume that this selection is perfect. For the proposed hybrid RF/FSO scheme we adopt the CCs and APs provided in Table 5.1 for all considered weather conditions. Optimizing the CCs and APs for the actual weather conditions would result in small additional performance gains at the expense of a considerable increase in signaling overhead (estimation of α, β, and K) and complexity (on–line optimization of CCs and APs). If the maximum RF and FSO transmit powers are not constrained (Figs. 7.3, 7.5, 7.6), we assign equal powers to both sub–channels as for the considered channel models the additional gains

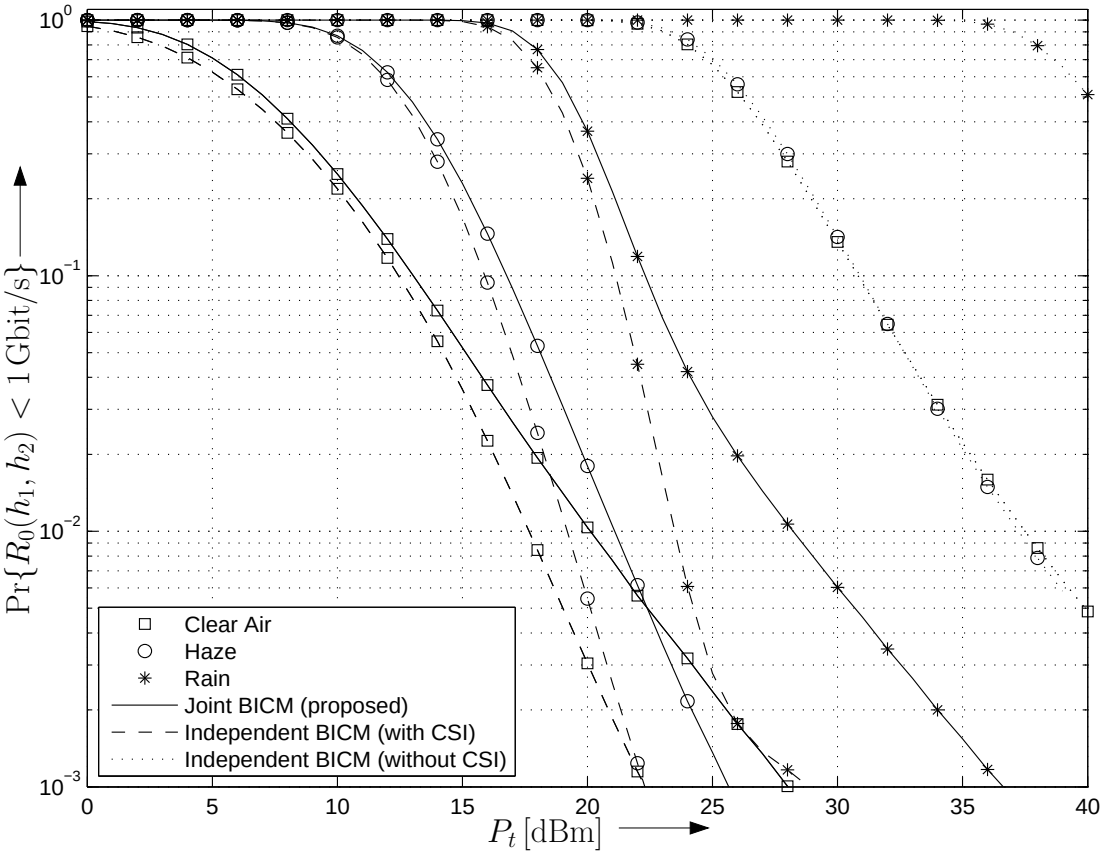

Figure 7.1: Outage probability for target rate of $R_{\text{target}} = 1$ Gbit/s for hybrid RF/FSO system with joint BICM (proposed), independent BICM with CSI at the transmitter, and independent BICM without CSI at the transmitter, respectively. 16–QAM in RF link and $L = 2.5$ km.

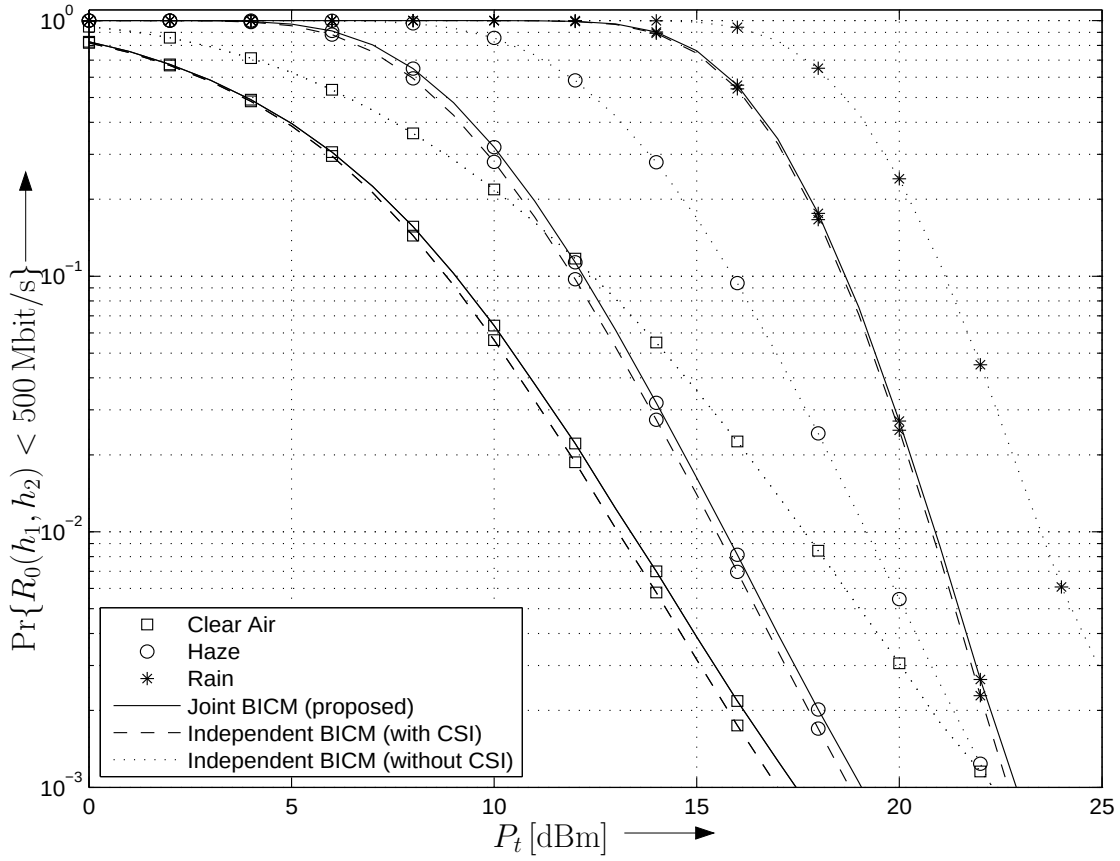

Figure 7.2: Outage probability for target rate of $R_{\text{target}} = 500$ Mbit/s for hybrid RF/FSO system with joint BICM (proposed), independent BICM with CSI at the transmitter, and independent BICM without CSI at the transmitter, respectively. 16–QAM in RF link and $L = 2.5$ km.

possible with the optimum power assignment in (4.25) are negligible.

Fig. 7.3 depicts the FER vs. P_t for hybrid RF/FSO systems with joint BICM (16–QAM, $R_c = 1/2$, $q = 7$, $N = 6$, cf. Table 5.1) and RC–SD (uncoded RF and uncoded FSO link), respectively. Clear air fog and moderate rain are considered for a link distance of $L = 2.5$ km. For comparison, we also show results for an uncoded FSO system, which yields a better performance than the uncoded RF system (not shown here). Note that all considered schemes have a data rate of 1 Gbit/s. Fig. 7.3 shows that joint BICM (solid lines) and RC–SD (dashed lines) have the same diversity orders and both schemes achieve a diversity gain compared to an uncoded FSO system (dotted lines) by exploiting the RF link. However, joint BICM substantially outperforms RC–SD. For example, at FER = 10^{-4} joint BICM yields gains of 4.3 dB,4.0 dB and 4.0 dB compared to RC–SD for clear air fog, and moderate rain, respectively. Furthermore, while joint BICM yields a performance similar to or better than that of uncoded FSO for all considered scenarios, RC–SD suffers from a 3 dB performance loss compared to uncoded FSO for moderate rain. For moderate rain the SNR in the FSO channel is substantially better than the SNR in the RF channel. Therefore, the simple RC–SD scheme chooses almost always the packets transmitted over the FSO link and the power assigned to the RF link is wasted. For Fig. 7.4 we adopted the same parameters as for Fig. 7.3. However, now the maximum RF power $P_{2,\max}$ was limited to 10 dBm, which is the legal limit in Japan and Australia, cf. [5], and for the proposed joint BICM scheme the RF and FSO transmit powers were assigned using the assignment scheme outlined in Section 4.3. For RC–SD the powers were assigned in a similar fashion. Note that the maximum FSO output power is not important here as it lies outside the considered P_t range, cf. [10]. The effect of RF power limitation is clearly visible in Fig. 7.4 as the FER curves for the two considered hybrid RF/FSO schemes are asymptotically parallel to the FER curves of the uncoded FSO link. Nevertheless, at FER = 10^{-3} the proposed joint BICM scheme yields a gain of 9.5 dB and 2.7 dB compared to

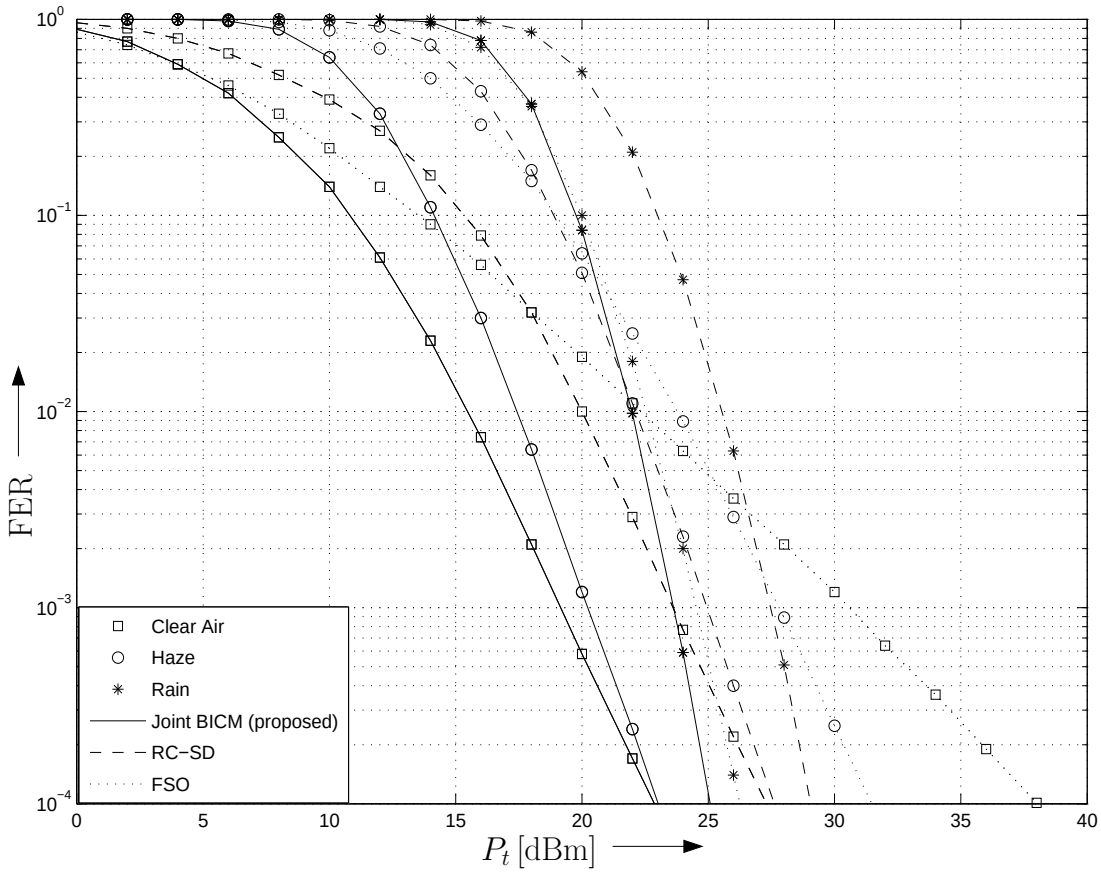

Figure 7.3: FER of hybrid RF/FSO system with joint BICM (16—QAM, $R_c = 1/2$, $q = 7$, $N = 6$, equal power for RF and FSO sub–channels, cf. Table 5.1) and RC–SD (uncoded RF and uncoded FSO sub–channels), respectively, and uncoded FSO. $L = 2.5$ km and data rate of 1 Gbit/s.

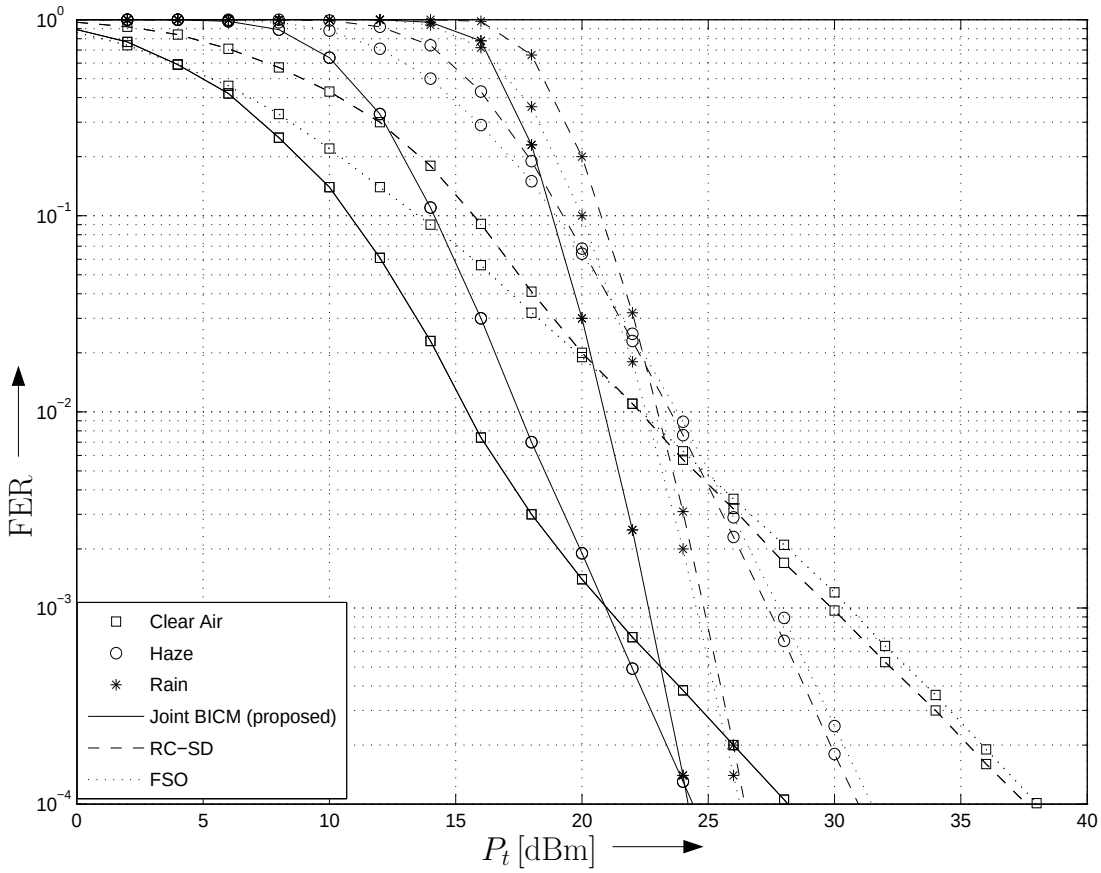

Figure 7.4: FER of hybrid RF/FSO system with joint BICM (16—QAM, $R_c = 1/2$, $q = 7$, $N = 6$, cf. Table 5.1) and RC–SD (uncoded RF and uncoded FSO sub–channels), respectively, and uncoded FSO. $P_{2,\max} = 10$ dBm, $L = 2.5$ km, and data rate of 1 Gbit/s.

the FSO link for clear air and moderate rain, respectively. It is also interesting to note that for moderate rain both joint BICM and RC–SD benefit from the power limitation in the RF link as more power is assigned to the FSO link which has a higher SNR. Therefore, the respective FER curves in Fig. **??** show an improved performance compared to those in Fig. 7.3. In Fig. 7.5, we show the FER of hybrid RF/FSO systems with joint BICM (16–QAM, $R_c = 1/4$, $q = 3$, $N = 12$, cf. Table 5.1) and RC–SD and the FER of pure FSO and RF systems. For RC–SD and the RF system 16–QAM is adopted for the RF link. For RC–SD we employed independent BICM for the RF and FSO sub–channels using the code with $R_c = 1/2$ and $q = 3$ from [29, Tab. 8.2-1]. The same code was also used for the pure FSO and RF systems. The data rate

of all four considered systems is 500 Mbit/s. In Fig. 7.5, performance under light fog and heavy rain is considered for $L = 2.5$ km. In light fog, the FSO system fails completely because of the high link attenuation. The RF system outperforms both hybrid systems by about 3 dB as the power assigned to the FSO link is essentially wasted in this case. Note that, in the considered P_t range, the FER curves for moderate and heavy fog are practically identical to those for light fog. In contrast, in heavy rain, the RF system fails and the FSO system has the best performance. The hybrid RF/FSO systems still achieve an acceptable performance and perform about 3 dB worse than the FSO system. Fig. 7.5 shows that because of its ability to provide protection against low SNR in one sub–channel by exploiting the high SNR in the other sub–channel, the proposed joint BICM approach offers a robust performance (without requiring CSI at the transmitter) even under extreme weather conditions.

Fig. 7.6 shows the FER of hybrid RF/FSO systems with joint BICM and RC–SD with 4–QAM in the RF link, respectively, and the FER of an FSO system. Haze and moderate rain scenarios are considered for $L = 2.5$ km. If full diversity is desired, the maximum code rate for joint BICM is $R_c = 1/3$, cf. Section 4.4. For joint BICM we adopt the code with $R_c = 1/3$, $q = 4$, and $N = 9$ from Table 5.1. For RC–SD the maximum free distance code with $R_c = 1/2$ and $q = 4$ from [29, Tab. 8.2-1] was used for the FSO link, while the RF link remained uncoded. The same code was also used for the FSO system. The data rate of all considered schemes is 500 Mbit/s. Fig. 7.6 confirms the superior performance of the proposed joint BICM approach as compared to RC–SD and FSO also for the case where the RF link supports a lower data rate than the FSO link.

Figure 7.7 shows the FER of hybrid FSO/RF with joint BICM (RF: 16–QAM, FSO: 16–QAM, $R_c = 1/2$) for code with different constraint length K and different assignment pattern N, according to the Table 5.1, for a distance of $L = 2.5$ Km, and a signal rate of 1 Gbit/s, under haze condition. Here we compare K from 3 to 7, with N between 4 and 6. Also, we compare the

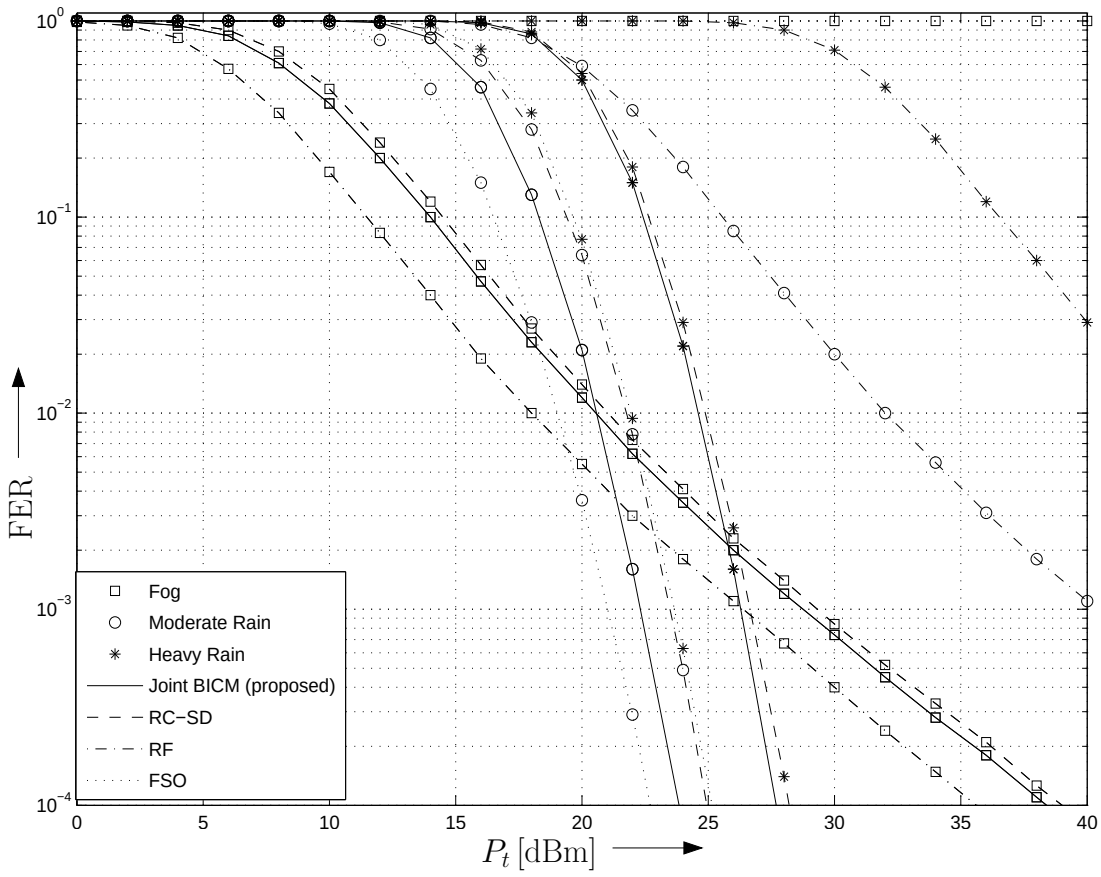

Figure 7.5: FER of hybrid RF/FSO system with joint BICM ($R_c = 1/4$, $q = 3$, $N = 12$, equal power for RF and FSO sub–channels, cf. Table 5.1) and RC–SD (16–QAM, $R_c = 1/2$, $q = 3$, in RF and FSO sub–channels), respectively, and coded RF ($R_c = 1/2$, $q = 3$) and coded FSO ($R_c = 1/2$, $q = 3$). $L = 2.5$ km and data rate of 500 Mbit/s.

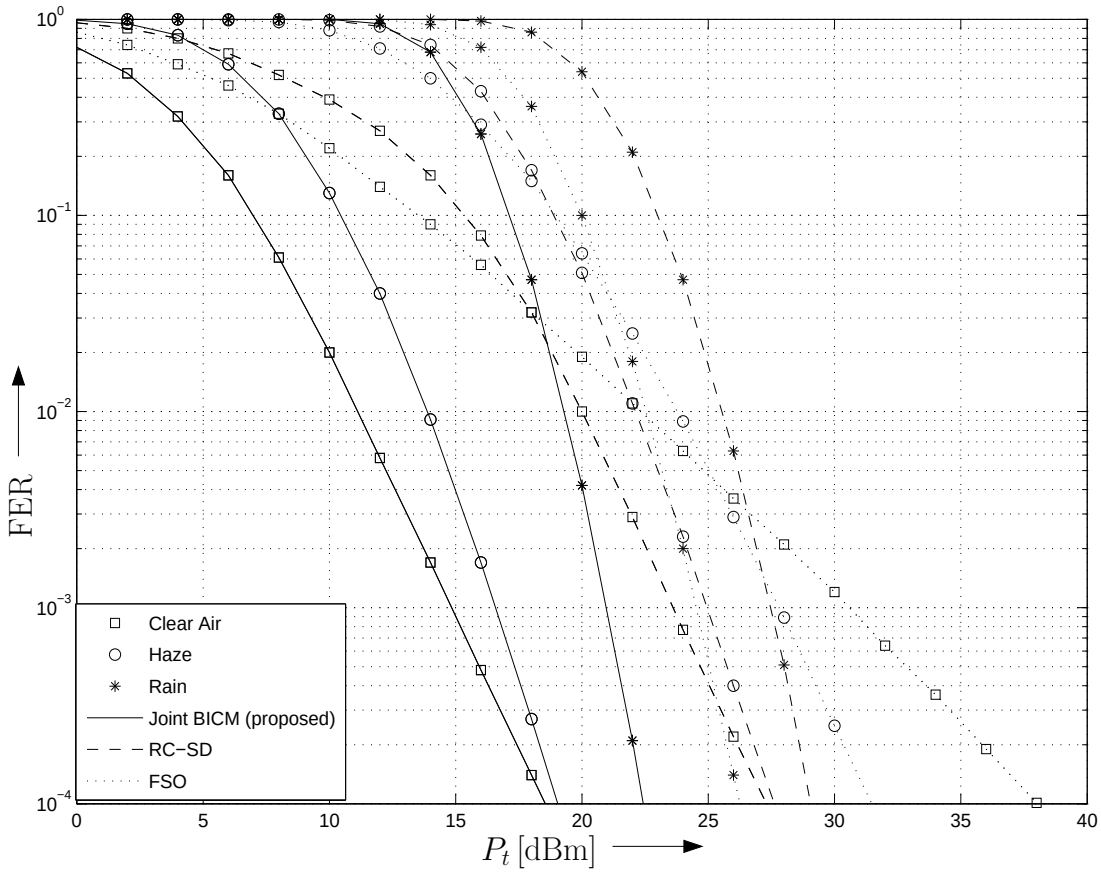

Figure 7.6: FER of hybrid RF/FSO system with joint BICM (4–QAM, $R_c = 1/3$, $q = 4$, $N = 9$, equal power for RF and FSO sub–channels, cf. Table 5.1) and RC–SD (uncoded RF sub–channel with 4–QAM, $R_c = 1/2$, $q = 4$ in FSO sub–channel), respectively, and coded FSO ($R_c = 1/2$, $q = 4$). $L = 2.5$ km and data rate of 1 Gbit/s.

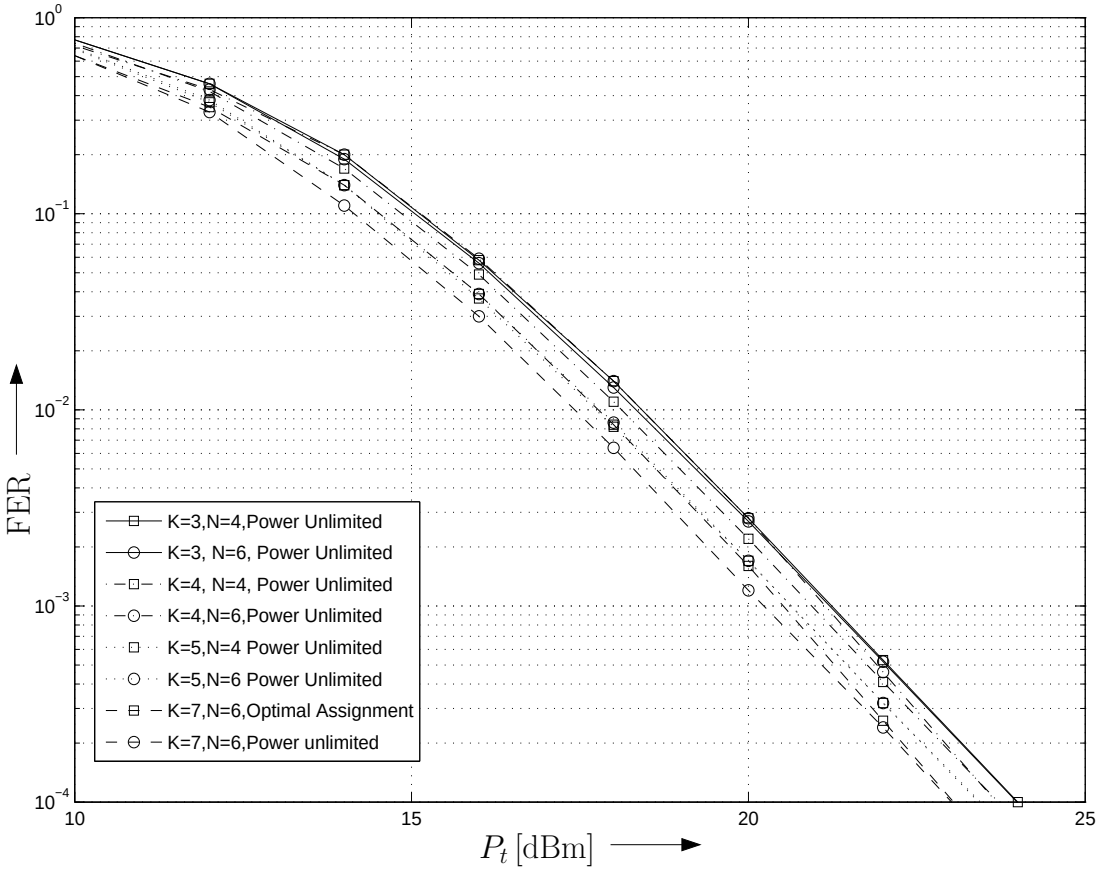

Figure 7.7: FER of hybrid RF/FSO system with joint BICM with different combination of constraint length, assignment pattern length and power limitation (coded RF subchannel with 16–QAM $R_c = 1/2$ and coded FSO subchannel $R_c = 1/2$). $L = 2.5$ km and data rate of 1 Gbit/s

cases between 2 power assignment schemes Optimal power ssignment vs. equal power assignment) for $K = 7$, $N = 6$. From the figure we observe that the asymptotic FERs for different scenarios are different. The length of assignment pattern has less effect than constraint length in terms of performance improvement. It is also interesting to see that two power assignment scenarios have similar performances asymptotically.

Chapter 8

Conclusions and Future Work

This chapter concludes the thesis with some general comments on the joint BICM hybrid system proposed in this work, followed by a discussion of possible future work for further investigation of the general our design.

8.1 Conclusions

In this thesis, a novel architecture for hybrid RF/FSO systems has been proposed. Joint BICM is applied to the bit streams transmitted over the RF link and the FSO link resulting in a robust hybrid system. The provided asymptotic performance analysis has shown that properly designed CCs and APs can exploit the diversity offered by the independent RF and FSO sub–channels. An efficient search procedure for corresponding CCs and APs has been provided. In this context, an upper bound for the code rate has been derived which guarantees the existence of codes achieving full diversity. Furthermore, the optimum power assignment if the maximum RF and/or FSO transmit power is limited has been discussed, and it has been shown that the RF link can be beneficial even if the maximum RF transmit power is limited. FER and cut–off rate results for typical system and channel parameters have confirmed the excellent performance of the proposed hybrid RF/FSO scheme for various weather conditions.

8.2 Recommendations for Future Work

We believe that the research work we initiated here on hybrid FSO/RF systems only scratches as the tip of the iceberg and many important questions remain to be answered. We list some recommendations for future work as follows:

- In the system model, we assume that the fading models are Gamma-Gamma distribution for the FSO channel and Rice fading for the RF channel. The union bound of CEP is derived based on these assumptions. However, it will be interesting to also take into account other fading models for both channels (for example, log-normal model for FSO for weak turbulence case). New union bounds for the CEP and new code/assignment pattern search algorithms should be derived for these channel models.

- Furthermore, we only discuss the case when a single transmitter and a single receiver is presented for each channel. We know multiple input multiple output (MIMO) systems can be applied to both systems. It would be interesting to investigate how our proposed design would change if MIMO was taken in to consideration .

- In the thesis, we use convolutional codes for channel coding. It is shown that turbo coding [48] has a performance approaching the Shannon limit. It is also suggested in [19] that BICM can be designed using binary parallel turbo coding. The high decoding complexity of turbo coding can be alleviated by using iterative decoding. It would be interesting to utilize turbo coding with BICM in our system and compare the CEP, the capacity, and the FER performance with the results with convolutional coding.

Bibliography

[1] H. Willeband and B. Ghuman. *Free Space Optics: Enabling Optical Connectivity in Today's Network*. Sams publishing, Indianapolis, 2002.

[2] D. Kedar and S. Arnon. Urban Optical Wireless Communication Networks: The Main Challenges and Possible Solutions. *IEEE Communications Magazine*, 42(5):2–7, 2004.

[3] Free Space Optics. http://www.free-space-optics.org.

[4] F. Giannetti, M. Luise, and R. Reggiannini. Mobile and Personal Communications in the 60 GHz Band: A Survey. *Wireless Personal Communications*, 10:207–243, July 1999.

[5] N. Guo, R. Qiu, S. Mo, and K. Takahashi. 60-GHz Millimeter-Wave Radio: Principle, Technology, and New Results. *EURASIP J. Wireless Commun. and Networking*, pages 1–7, January 2007.

[6] L. Andrews, R. Phillips, and C. Hopen. Laser Beam Scintillation with Applications. *EURASIP J. Wireless Commun. and Networking*, 2001.

[7] M. Al-Habash, L. Andrews, and R. Phillips. Mathematical Model for the Irradiance Probability Density Function of a Laser Beam Propagating Through Turbulent Media. *Optical Engineering*, 40(8):1554–1562, August 2001.

[8] P. Vasconcelos and L. Correia. Fading Characterization of the Mobile Radio Channel at the Millimetre Waveband. In *Proc. IEEE Vehicular Technol. Conf.* (VTC), pages 999–1003, May 1997.

[9] J. Schöther. Fading Characterization of the Mobile Radio Channel at the Millimetre Waveband. Ist-2001-32686, Broadway, 2001.

[10] I. Kim and E. Korevaar. Availability of Free Space Optics (FSO) and Hybrid FSO/RF Systems. *Optical Wireless Communications IV*, August 2001.

[11] A. Akbulut, G. Ilk, and F. Ari. Design, Availability and Reliability Analysis on an Experimental Outdoor FSO/RF Communication System. In *Proc. Intern. Transparent Optical Networks Conf. (ICTON)*, pages 403–406, July 2005.

[12] J. Derenick, C. Thorne, and J. Spletzer. On the Deployment of a Hybrid Free-space Optic/Radio Frequency (FSO/RF) Mobile Ad-hoc Network. In *Proc. IEEE Intern. Conf. Commun. (ICC)*, pages 3990–3996, August 2005.

[13] S. Bloom and W. Hartley. The Last-Mile Solution: Hybrid FSO Radio, May 2002. White Paper, AirFiber,. Inc., 802-0008-000 M-A1.

[14] E. Leitgeb and M. Gebhart. High Availability of Hybrid Wireless Networks. In *Proc. SPIE*, volume 5465, pages 238–249, 2004.

[15] H. Wu, B. Hamzeh, and M. Kavehrad. Achieving Carrier Class Availability of FSO Link via a Complementary RF Link. In *Proc. Asilomar Conf. Signals, Systems and Computers*, volume 2, pages 1483–1487, November 2004.

[16] S. Vangala and H. Pishro-Nik. A Highly Reliable FSO/RF Communication System Using Efficient Codes. In *Proc. IEEE Global Telecommun. Conf. (Globecom)*, pages 2232–2236, Washington, DC, November 2007.

[17] E. Malkamäki and H. Leib. Coded Diversity on Block-Fading Channels. *IEEE Trans. Inform. Theory*, 45:771–781, March 1999.

[18] R. Knopp and P. Humblet. On Coding for Block Fading Channels. *IEEE Trans. Inform. Theory*, 46:189–205, January 2000.

[19] G. Caire, G. Taricco, and E. Biglieri. Bit-Interleaved Coded Modulation. *IEEE Trans. Inform. Theory*, 44:927–946, May 1998.

[20] A. Guillen i Fabregas and G. Caire. Coded Modulation in the Block-Fading Channel: Coding Theorems and Code Construction. *IEEE Trans. Inform. Theory*, 52:91–114, January 2006.

[21] Y. Leung, S. Wilson, and J. Ketchum. Multifrequency Trellis Coding with Low Delay for Fading Channels. *IEEE Trans. Commun.*, 41:1450–1459, October 1993.

[22] M. Chiani, A. Conti, and V. Tralli. Further Results on Convolutional Code Search for Block-Fading Channels. *IEEE Trans. Inform. Theory*, 50:1312–1318, June 2004.

[23] M. Uysal, J. Li, and M. Yu. Error Rate Performance Analysis of Coded Free-Space Optical Links over Gamma-Gamma Atmospheric Turbulence Channels. *IEEE Trans. Wireless Commun.*, 5(6):1229–1233, June 2006.

[24] E. Bayaki, R. Schober, and R. Mallik. Performance Analysis of Free-Space Optical Systems in Gamma-Gamma Fading. In *Accepted for Presentation at the IEEE Global Telecommun. Conf. (Globecom), [Online] http://www.ece.ubc.ca/∼ehsanb/GC08.pdf*, 2008.

[25] S. Muhammad, P. Köhldorfer, and E. Leitgeb. Channel Modeling for Terrestrial Free Space Optical Links. In *Proc. IEEE Intern. Conf. Transparent Optical Networks (ICTON)*, pages 407–410, July 2005.

[26] I. Kim, B. McArthur, and E. Korevaar. Comparison of Laser Beam Propagation at 785 nm and 1550 nm in Fog and Haze for Optical Wireless Communications. In *Proc. SPIE*, volume 4214, pages 26–37, 2001.

[27] X. Zhu and J. M. Kahn. Free-Space Optical Communication Through Atmospheric Turbulence Channels. *IEEE Trans. Commun.*, 50(8):1293–1300, August 2002.

[28] J. Goodman. *Statistical optics*. John Wiley and Son, 1985.

[29] J. Proakis. *Digital Communications*. McGraw–Hill, New York, 2000.

[30] Lianne Caetano and Sheung Li. Benefits of 60 GHz: Right Frequency, Right Time. SiBEAM Inc., November 2005.

[31] ISM band. http://en.wikipedia.org/wiki/ISMband.

[32] IEEE 802.11. http://en.wikipedia.org/wiki/802.11.

[33] HIPERLAN. http://en.wikipedia.org/wiki/HIPERLAN.

[34] P. Smulders. Exploiting The 60 GHz Band For Local Wireless Multimedia Access: Prospects and Future Directions . *IEEE Communication magazine*, 40(1):140–147, January 2002.

[35] K. Gosseand K. Taffin and N. Whinnett. Propagation and Deployment of Mobile Broadband Systems in The 60 GHz Band. Technical report, Motorola CRM internal, March 1999. v.1.0.

[36] P. Lusina. Ka-Broadband Satellite Communication using Cyclostationary Parabolic Beamforming. Master's thesis, Queen's University, Kingston, Ontario, Canada, August 1997.

[37] S. Vangala and H. Pishro-Nik. Optimal Hybrid RF-wireless Optical Communication for Maximum Efficiency and Reliability. In *Information sciences and systems, 2007. CISS '07. 41st Annual Conference on* , pages 684–689, March 2007.

[38] S. Milner and C. Davis. Hybrid Free Space Optical/RF Networks for Tactical Operations. In *Proc. IEEE Military Commun. Conf. (MILCOM)*, pages 409–415, Monterey, CA, October 2004.

[39] H. Pishro-Nik and H. F. Fekri. Results on Non-uniform Error Correction Using Low-Density Parity Check Codes. In *Proc. IEEE global telecommun. conf. (Globecom)* , pages 2041–2045, December 2003.

[40] A. A. Farid and S. Hranilovic. Outage Capacity Optimization for Free-Space Optical Links With Pointing Errors. *IEEE J. Lightwave Techn.*, pages 1702–1710, July 2007.

[41] W. Schäfer. Channel Modelling of Short-Range Radio Links at 60 GHz for Mobile Intervehicle Communication. In *Proc. IEEE Veh. Techn. Conf. (VTC)*, pages 314–319, St. Louis, USA, May 1991.

[42] Z. Wang and G. Giannakis. A Simple and General Parameterization Quantifying Performance in Fading Channels. *IEEE Trans. Commun.*, 51:1389–1398, August 2003.

[43] I. Gradshteyn and I. Ryzhik. *Table of Integrals, Series, and Products*. Academic Press, New York, 2000.

[44] S. Yong and C.-C. Chong. An Overview of Multigigabit Wireless through Millimeter Wave Technology: Potentials and Technical Challenges. *EURASIP J. Wireless Commun. and Networking*, pages 1–10, January 2007.

[45] T. Moon and W. Stirling. *Mathematical Methods and Algorithms for Signal Processing*. Prentice Hall, New York, 2000.

[46] J. Wolf and A. Viterbi. On the Weight Distribution of Linear Block Codes Formed From Convolutional Codes. *IEEE Trans. Commun.*, 44:1049–1051, September 1996.

[47] I. Sason and I. Goldenberg. Coding for Parallel Channels: Gallager Bounds and Application to Turbo-Like Codes. *IEEE Trans. Inform. Theory*, 53:2394–2428, July 2007.

[48] C. Berrou and A. Glavieux. Near Optimum Error Correcting Coding and Decoding: Turbo-Codes. *IEEE Trans. Commun.*, 44(10):1261–1271, October 1996.